공학석사학위논문

복합열전달을 고려한 고압터빈 막냉각홀 배열 다중정확도 최적화

Variable Fidelity Optimization of Film Cooling Hole Arrangements on High Pressure Turbine Considering Conjugate Heat Transfer

2017 년 8 월

서울대학교 대학원

기계항공공학부

김 윤 기

복합열전달을 고려한 고압터빈 막냉각홀 배열 다중정확도 최적화

Variable Fidelity Optimization of Film Cooling Hole Arrangements on High Pressure Turbine Considering Conjugate Heat Transfer

지도교수 이 관 중

이 논문을 공학석사 학위논문으로 제출함

2017 년 8 월

서울대학교 대학원
기계항공공학부
김 윤 기

김윤기의 공학석사 학위논문을 인준함

2017 년 6 월

위 원 장 金奎弘

부위원장 李管中

위 원 황원태

ABSTRACT

Variable Fidelity Optimization of Film Cooling Hole Arrangements on High Pressure Turbine Considering Conjugate Heat Transfer

Yoonki Kim

Mechanical and Aerospace Engineering

The Graduate School

Seoul National University

Conjugate heat transfer (CHT) should be taken into account when analyzing heat transfer in high pressure turbine (HPT) to improve the accuracy of the simulation because film cooling is used to reduce the convective heat transfer into the blade and temperature potential which drives conduction by coolant film extracted from holes. However, Research of film cooling hole array optimization have been conducted under the adiabatic condition due to high computation burden in CHT analysis. Moreover, optimization considering CHT has been restrictively attempted on relatively simple problem such as single hole shape optimization problem. In this study, film cooling hole arrangement is optimized by considering CHT effects. In an effort to reduce computation load, EI-based efficient global optimization (EGO) algorithm coupled with hierarchical Kriging (HK) model is implemented. There, however, have been still several ambiguities to be clarified when applying the HK model to hole array optimization problem for practical utilization. The first is the existence of optimal high to low fidelity sample ratio to reduce the computational cost.

The second is whether the HK model can produce converged result irrespective of the different high-to-low fidelity sample ratio. All the analyses of the ambiguity-clarification are conducted under the adiabatic condition. As a result, HK model not only produce the consistent and reliable optimization result but also reduce the CPU time at the similar level, 40%, irrespective of the different high-to-low fidelity sample ratios. Based on the adiabatic analysis-based optimization results, CHT-based optimization is conducted with 3-level HK model. Computation time decreases by 76.45% compared to CHT-only optimization. Furthermore, the film cooling hole arrangement shows substantially different configuration from adiabatic analysis-based optimization results. Specifically, although the second array shape is similar to the adiabatic result, the third hole arrangement has curvature towards the leading edge like a parabola. This resultant hole array configuration is shown to be the best combination of inner cooling components and film cooling hole locations, which make the inner and outer coolant cover the nozzle surface as much as possible. The detailed reasons why the hole arrangements are determined are discussed by investigating the pressure, velocity contours, and streamlines. As a result, the nozzle surface temperature decreases by 49.64 K and average overall film cooling effectiveness (ϕ) increases by 0.058 compared to those of baseline. The method used in this study is promising in terms of handling highly-nonlinear or high-computing required problems.

keywords : Aircraft gas turbine, High pressure turbine, Conjugate heat transfer analysis, Hierarchical Kriging model, Film cooling hole array optimization

***Student Number* : 2015-22733**

LIST

LIST OF FIGURES

LIST OF TABLES

I. Introduction

High pressure turbine (HPT) operates under extremely high temperature. Especially, the nozzle guide vanes (NGVs), which are located right behind the combustor, are the components of HPT exposed to the most severe operating condition. There also have been a lot of attempts to increase the turbine inlet temperature further for the improvement of gas turbine efficiency. For this reason, NGVs are vulnerable to wear out from thermal stress, so turbine cooling techniques have drawn serious attention for the past few decades.

Turbine cooling techniques are generally divided into two categories—internal cooling and external cooling. First, internal cooling uses conduction effect of coolant with substantially lower temperature than the operating temperature. Specific amount of coolant flows through the internal cooling passage installed in the blade. On the other hand, external cooling uses several numbers of holes which are drilled on the blade surface, connecting the internal cooling passage to main passage. Since the coolant extracted from the internal cooling passage covers the blade surface like thin film, this external cooling technique is also called film cooling.

Film cooling techniques have been widely implemented in gas turbine design since their introduction. With the advancement of computing power and development of efficient numerical methods in computational fluid dynamics (CFD), a number of works have already been conducted on improving film cooling performance. For instance, the optimization of a film cooling hole shape has been numerically attempted in recent years [1-3]. Application of the optimized hole shape to a real gas turbine,

however, has inherent limitations because novel film cooling hole shapes are geometrically too complicated to manufacture and susceptible to wearing out during operation.

After carefully considering these limitations, recent research moved towards the optimization of the hole arrangement [4-8] rather than the optimization of single film cooling hole. Especially, Lee [7] proposed a high-fidelity affordable design procedure for film cooling hole array optimization. Since then, Lee [8] improved the procedure which can consider uncertainty—manufacturing tolerance. These studies noted that the hole arrangement can improve cooling effectiveness without any modification of the hole shape. Moreover, from the perspective of manufacturing cost, optimizing the hole arrangement is more cost efficient than altering the hole shape.

Despite recent advancements of numerical techniques in optimization and CFD, most of the preceding studies have been conducted under adiabatic conditions not considering conjugated heat transfer (CHT) due to the huge computational burdens. Some previous studies [9, 10], however, indicate that the CHT-based optimization would produce quite different results compared with those from the adiabatic analysis-based optimization because the conduction from the internal cooling passages can significantly influence on the surface temperature. Nevertheless, considering the available computing resources in common design environments, it is almost impossible to attempt CHT-based optimization unless an alternative and novel design technique that can significantly reduce the overall computing time is introduced.

In order to circumvent the huge computation resources required for the optimization, variable fidelity modeling (VFM) is suggested as one of viable ideas in this study. The VFM is the one of surrogate modeling methods, where various degrees

of fidelity information are used to construct the surrogate model efficiently. The basic idea behind VFM is that the general tendency of a model is constructed based on the large number of low-fidelity information, while the accuracy of model is tuned using several number of high-fidelity information. That is to say, the effectiveness of VFM comes from reducing the number of expensive high-fidelity computations by utilizing low-fidelity computation. The level of fidelity can be chosen in various manners: the mesh density (dense grid vs. coarse grid), the fidelity of the solver (Navier-Stokes vs. Euler or Potential solver) to name a few. In this study, Hierarchical Kriging (HK) model is employed as a VFM. There are several preceding studies using HK model. Zhong-Hua Han et al. [11] demonstrated that HK model could yield more accurate prediction compared with other modeling methods, where the pitching moment coefficients of RAE 2822 airfoil and aerodynamic data of 3D industrial aircraft configuration are used. In addition, Wilke [12] presented the efficient optimization results for helicopter rotor blade design using HK model, where fidelity level was extended from low-mid (2-level) to low-mid-high (3-level). Furthermore, single- and multi-objective problems were also considered. From this optimization procedure, reasonably optimized rotor geometry was obtained with substantially reduced computation time.

However, to practically utilize the HK model in HPT optimization and directly apply the HK model to film cooling hole array optimization considering CHT, there are some ambiguous points that need to be clarified under the adiabatic condition. First, it is unclear whether there is a best high-to-low fidelity initial sample ratio. Most previous studies chose the number of high- and low-fidelity initial samples arbitrarily. However, because the hole arrangement optimization conducted in this study is a

highly non-linear problem, this ambiguity-clarification can offer a practical guideline for CHT-based optimization. Second, it should be verified whether the problem converges to the same value regardless of different high-to-low fidelity initial sample ratios when using the HK model. Unless the obtained results are similar when compared to the high-fidelity only optimization, the HK model would lose its validity in the general optimization problem. In addition, the time reduction and resultant geometries of optimization are thoroughly compared and investigated to clarify the ambiguous points in the HK-based variable fidelity optimization. For the efficiency of calculation with keeping the accuracy of simulation, all the calculations related to the ambiguity-clarifications are conducted using simplified nozzle geometry, which has film cooling hole arrays only at the nozzle pressure side and inner cooling passages excepting other inner cooling components such as rib turbulators, impinging holes, pedestals, etc.

Based on the results of adiabatic analysis-based optimization, the film cooling hole arrangement is optimized considering the conjugate heat transfer. Specifically, CHT-based optimization is conducted with 3-level HK model which is composed of 2-level adiabatic analysis-based HK model and CHT initial samples applied on the same number of the best case obtained from the adiabatic analysis-based optimization. With 3-level HK model, optimization is progressed with the same optimization framework of adiabatic case. Additionally, contrary to the adiabatic analysis-based optimization, fully cooled nozzle geometry is used for the CHT-based optimization because blade cooling is significantly influenced by the conduction effect as well as convection effect.

The goals of this study are suggesting the affordable CHT-based optimization framework of film cooling hole arrangement. With this framework, the efficiency of framework applied with HK model is investigated compared to the optimization with fully CHT analyses. In addition, the differences of resultant geometries between CHT- and adiabatic analysis-based optimization are demonstrated and what makes the CHT resultant geometries different compared to that of adiabatic condition is also argued by investigating the pressure, velocity contours, and streamlines in inner cooling passage.

In summary, this paper is largely divided into two parts. One is ambiguity-clarification part, which is conducted for applying the HK model to film cooling hole array optimization practically under the adiabatic condition. The other part is CHT-based optimization which is conducted with the 3-level of HK model. All the results are thoroughly discussed, especially focusing on the CPU time reduction, geometries of film cooling hole array, and nozzle surface temperature distribution.

II. Methodology

A. Problem Definition

In the previous research [5], novel shape functions are suggested to present hole arrangements in severely restricted areas. The shape functions including 9 variables, R_{1x}, R_{1y}, R_{1g}, R_{1c}, R_{1s}, R_{2x}, R_{2g}, R_{2c}, and R_{2s}, are also used to generate the hole arrays in this study. In more detail, R_{1x} and R_{1y} fix the lowest hole location in the design space for ROW1. R_{1g} which defines the gradient of hole array fixes the highest hole location. At last, R_{1c} and R_{1s} which mean curvature and spacing of hole array determine the rest of hole location. Figure 1 describes the design spaces of the optimization and definitions of each variable. The reader can obtain more detailed information about the variables and domain in Ref. [5].

The performance of the film cooling is assessed by the average surface temperature of the nozzle pressure side. Therefore, single-objective optimization problem is defined to minimize the average temperature of the nozzle pressure side. Additionally, 3 constraints are imposed. The optima should have lower temperature compared with the baseline. The rest 2 constraints are imposed to the mass flow rate. With the increase of the mass flow of the coolant, the cooling performance of the film cooling increases, but the entire turbine performance decreases. Accordingly, it is reasonable to restrict the overall mass flow rate of the coolant.

Objective Min. $T_{avg} = \frac{1}{A_{PS}} \iint_{A_{ps}} T_W(s) ds$

Constraints

$T_{avg} \le T_{avg\_base}$, $\dot{m}_{total\_base} \ge \dot{m}_{total}$, $\dot{m}_{hole\_base} \ge \dot{m}_{hole}$

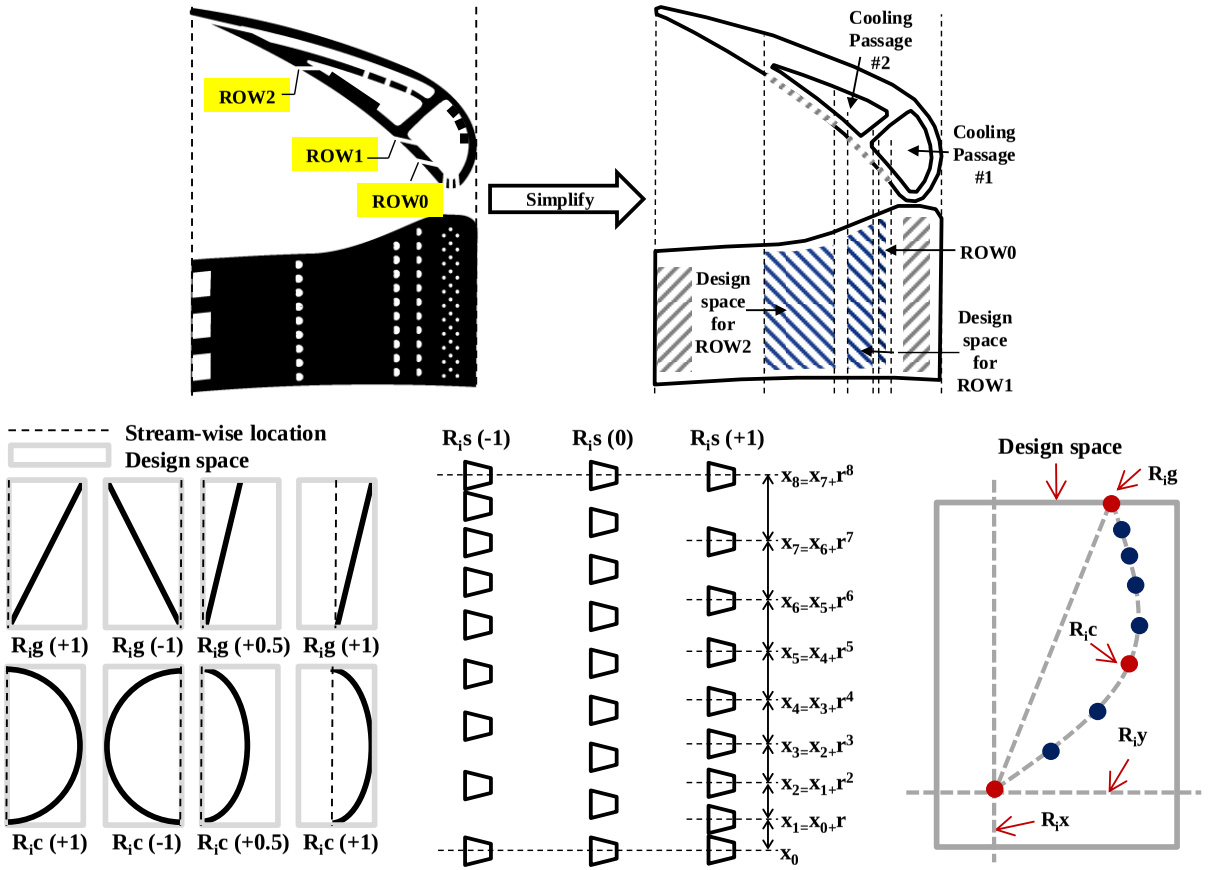

Fig. 1 Design spaces and 9 design variables [5]

B. Numerical Approach

The nozzle of the 1st stage high pressure turbine of a 10,000 lbf-class aircraft gas turbine engine is chosen as a reference model. The model has 56 nozzles whose average span length is approximately 20 mm, and the mean radius of the turbine is 275 mm. Also, the axial and true chord lengths of the nozzle are set to be 23 mm and 41 mm, respectively. In addition, the flow inlet and exit angle are given zero and 74°. The inlet Reynolds number is about 3.9×10^{5}, the outlet Reynolds number is about 2.1×10^{6} based on the true chord length. The detailed specification of the turbine is summarized in Rhee et al. [6].

At the HPT nozzle, 2 internal cooling passages and 3 arrays of film cooling holes are installed for the nozzle cooling. The 3 arrays are named ROW0, ROW1 and ROW2 in order from the leading edge, and the "pressure side" stands for the domain from ROW0 to the trailing edge in this study. Among these cooling components on the pressure side, the optimization target is the 2 arrays of film cooling hole—ROW1 and ROW2. All the film cooling holes have the same shape but different injection angles. The injection angle is 30° with respect to the nozzle surface, with the exception of 34° in ROW0. The diffusion angle is 10° in the span-wise direction, and the diffusion location is on the 1/3 point of the hole length from the hole inlet, as described in Fig. 2.

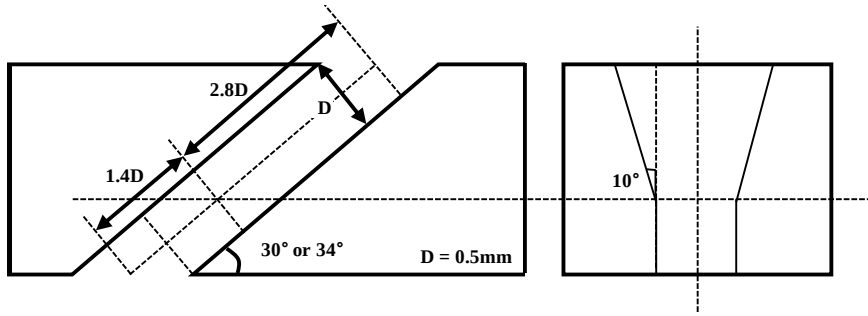

Fig. 2 Cooling configuration

For both adiabatic and CHT analyses, the compressible steady Reynolds-averaged Navier-Stokes (RANS) equations of Eqs. (1) ~ (3) are used as governing equations. Contrary to the adiabatic analysis, the conservation of energy equation (Eq. (8)) should be taken into account with the thermal properties of the solid domain, CMSX4.

More in detail, equations (1) and (2) are the Reynolds-averaged transport equations. Eq. (3) is Reynolds-averaged energy equation. For substituting the thermal conductivity term (λ), modified Eucken model expressed in Eq. (4) is used [13]. In order to use this model, the specific heat (c_p/R) should be determined. Since the operating condition is severely extreme, the thermodynamic properties such as conductivity or heat capacity are determined depending on the temperature. In this study, the 4th order polynomial expressed as Eq. (5) is employed. This polynomial model has 0.9999 of R-square value [14]. Additionally, the dynamic viscosity is obtained from the Sutherland formula as Eq. (6). Sutherland's constant is 110.4 K. In addition, μ_{ref}, T_{ref} and n are reference viscosity, temperature and temperature exponent, which have 1.716e-5 Pa·s, 273.15 K and 1.5, respectively. Furthermore, the turbine inlet temperature is given as a parabolic form with an average temperature of

1,673 K and maximum temperature of 1,830 K. In this range of temperature, the ideal gas assumption can be held and the ideal gas equation of state is employed as in Eq. (7). The density is obtained from the ideal gas law and c_p is given as a function of temperature only. w is the molecular weight, p_{abs} is the absolute pressure and R is the universal gas constant. In Eq. (8), ρ , h , and λ is density, enthalpy, and thermal conductivity of the material, respectively.

For turbulence model, the k-ω shear stress transport (SST) model is employed. The SST model is known to yield better prediction for near-wall turbulent flow, especially with adverse pressure and separation [15]. In addition, Lee et al. [16] and Ayoubi et al. [17] demonstrated that the SST model shows good performance in the turbine heat transfer and film cooling hole problem. The turbulent intensity is set to be 5%. All the analyses are conducted on ANSYS CFX 16.2, which uses the element-based finite volume method (FVM) and algebraic multi-grid (AMG) coupled solver [18].

$$\frac{\partial \rho}{\partial t} + \frac{\partial}{\partial x_j}(\rho U_j) = 0 \tag{1}$$

$$\frac{\partial \rho U_i}{\partial t} + \frac{\partial}{\partial x_j}(\rho U_i U_j) = -\frac{\partial P}{\partial x_i} + \frac{\partial}{\partial x_j}(\tau_{ij} - \rho\overline{u_i u_j}) \tag{2}$$

$$\frac{\partial \rho h_{tot}}{\partial t} - \frac{\partial P}{\partial t} + \frac{\partial}{\partial x_j}(\rho U_j h_{tot}) = \frac{\partial}{\partial x_i}\left(\lambda \frac{\partial T}{\partial x_i} - \rho\overline{u_j h}\right) + \frac{\partial}{\partial x_j}\left[U_i(\tau_{ij} - \rho\overline{u_i u_j})\right] \tag{3}$$

$$\frac{\lambda}{\mu(c_p - R_0)} = 1.32 + \frac{1.77}{\left(c_p \big/ R_0 - 1\right)} \tag{4}$$

$$\frac{c_p}{R_0} = 3.53881 - 6.77619e^{-4}T + 2.26946e^{-6}T^2 - 1.44141e^{-9}T^3 + 2.91951e^{-13}T^4 \tag{5}$$

$$\frac{\mu}{\mu_{ref}} = \frac{T_{ref} + S}{T + S}\left(\frac{T}{T_{ref}}\right)^n \tag{6}$$

$$\rho = \frac{wP_{abs}}{R_0 T}, \quad dh = c_p dT, \quad c_p = c_p(T) \tag{7}$$

$$\frac{\partial(\rho h)}{\partial t} = \nabla \cdot (\lambda \nabla T) \tag{8}$$

The specific boundary conditions for fluid analysis are given in Table 1, which is equivalent to the adiabatic and CHT analyses. Figure 3 and 4 illustrate the overall boundary conditions and interface settings for adiabatic and CHT analyses, respectively. In addition, the thermodynamic material properties of nozzle, CMSX4, are shown in Table 2.

Table 1 Boundary conditions

Locations	Properties	Mean values
Main passage inlet	Total pressure	30.685 bar
	Average total temperature	1,673 K
Main passage outlet	Static pressure	15.650 bar
Cooling passage inlet	Total pressure	32 bar
	Total temperature	837 K
Cooling passage outlet	Total pressure	31.9 bar

Table 2 Thermodynamic properties of CMSX4

Thermodynamic properties		Value
Equation of state	Molar mass	58.69 Kg / kmol
	Density	8691.5 Kg /m^3
Transport properties	Thermal conductivity	{0.019374*(T-273.15)+8.471358}Kg·m / s^3 ·K
Specific heat capacity		860 J/kg·K

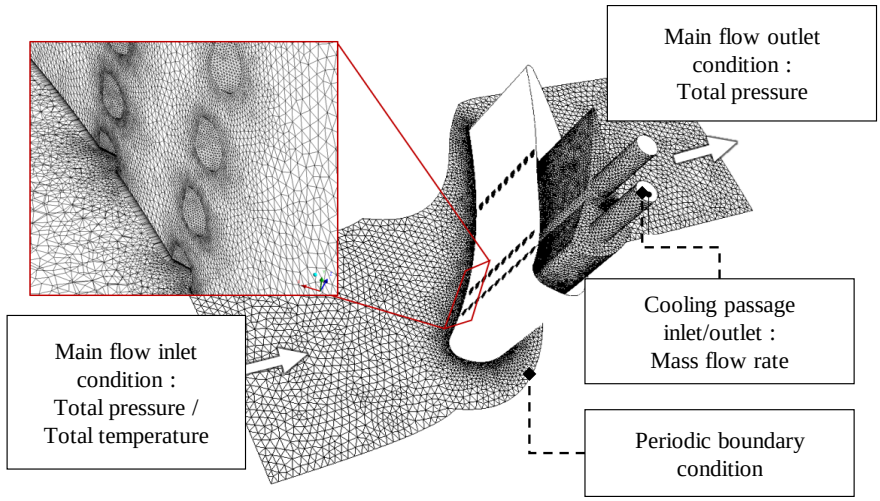

Fig. 3 Adiabatic boundary conditions

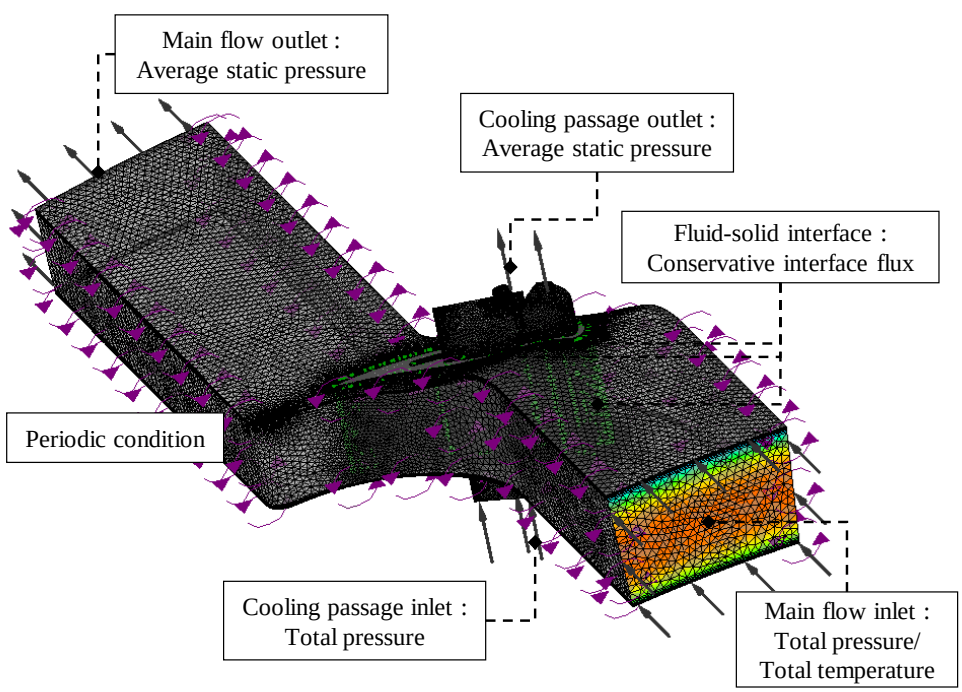

Fig. 4 Conjugate heat transfer boundary conditions and interface information

C. VFM Coupled with Efficient Global Optimization (EGO)

VFM is a concept of surrogate modeling using various degrees of fidelity information. It was firstly suggested for the purpose of reducing high computation burden. When explaining the construction process of VFM, it builds the low-fidelity surrogate model at first to mimic the global trend. Subsequently, the high-fidelity calculations are conducted and low-fidelity surrogate model is corrected by using high fidelity information. Moreover, the high-fidelity information is utilized additionally in refinement process to enhance the accuracy of variable fidelity model.

Despite the existence of various kind of surrogate model such as polynomial, radial basis functions, and Kriging, the VFM originated from Kriging is particularly employed in this study. There has already existed various Kriging-based VFM available such as correction-based method, cokriging method, and Hierarchical Kriging VFM [9]. Before the detailed introduction of HK model, correction-based and cokriging methods are presented briefly in advance.

Correction-based VFM is the most popular method. The word "correction" is regarded as "scaling function" or "bridge function", which can be multiplicative, additive, or multiplicative/additive. Examining one by one, multiplicative scaling function is used to locally tune the low-fidelity function. In contrast, additive method is to globally correct the low-fidelity function. It is known that additive method can predict surrogate model more accurately and robustly than multiplicative method for most of the cases. After then, the hybrid approach which mixes the above two methods is suggested.

Cokriging method is firstly proposed in the geostatistics and widely used for spatial interpolation. The basic idea of this method is that Kriging model is not only used, but the second Kriging model is also constructed to formulate the difference between low and high fidelity outputs while including multiplicative scaling factor. The scaling factor is continuously tuned when every second Kriging is constructed.

Compared to these two methods, correction-based VFM is simple and robust, but less accurate than cokriging method. On the other hand, error such as mean-square error (MSE) can be provided easily by cokriging method. Error estimation is utilized for the refinement of surrogate model, which would be discussed in later chapter.

Hierarchical Kriging (HK) model is employed in this study. This model was suggested by Zhong-Hua Han et al. [11] based on motivation to develop a simple and robust method as correction-based Kriging and also accurate as cokriging-based VFM. Therefore, it is particularly suitable to handle the highly-nonlinear or highly-uncertain problems such as film cooling hole array optimization problem. In addition, contrary to the other ordinary Kriging model which uses low-order polynomials as a global trend function, HK model is constructed using another low-fidelity Kriging model scaled by multiplicative factor as a global function. This process seems hierarchical, so this method is called hierarchical Kriging.

For further understanding procedures of expansion of HK model, mathematical formulae should be analyzed. The formulae are defined in hierarchical step—Kriging for low-fidelity function, HK model for high-fidelity function.

$$Y_{lf}(x) = \beta_{0,lf} + Z_{lf}(x) \xrightarrow{predictor} \hat{y}_{lf}(x) = \beta_{0,lf} + r_{lf}^{T}(x) R_{lf}^{-1}(y_{S,lf} - \beta_{0,lf}1) \qquad (9)$$

Equation (9) is Kriging for low-fidelity function. Z_{lf} is stationary random process. $\beta_{0,lf}$ is unknown constant which is defined as the mean of the stochastic process. R, r are correlation matrix and vector representing the correlation between the observed points, respectively. Examining the expansion process of Kriging model more in detail, the linear predictor $\hat{y}(x)$ at untried x is defined as Eq. (10). The best linear unbiased predictor (BLUP) which indicates the predictor of HK model is built in this step. The key factor to determine the BLUP is obtaining vector of weight coefficients w. y_S is high-fidelity sample data, and Y_S is corresponding random quantities.

$$\hat{y}(x) = w^T y_S \tag{10}$$

$$\begin{aligned} &MSE[\hat{y}(x)] = E\left[\left(w^T Y_S - Y(x)\right)^2\right] \\ &subject\ to: E\left[\sum_{i=1}^{n} w^{(i)} Y(x^{(i)})\right] = E[Y(x)] \end{aligned} \tag{11}$$

$$\hat{y}(x) = \begin{bmatrix} r(x) \\ \hat{y}_{lf}(x) \end{bmatrix}^T \begin{bmatrix} R & F \\ F^T & 0 \end{bmatrix}^{-1} \begin{bmatrix} y_S \\ 0 \end{bmatrix} \tag{12}$$

Weight coefficient vector w is obtained from the result of this constrained minimization problem as in Eq. (11). Constrained minimization problem can be solved analytically by applying the Lagrange multiplier. After determining w, Eq. (10) can be expressed in matrix form such as Eq. (12). When calculating inverse matrix of Eq. (12), the BLUP expressed in the right hand side of Eq. (9) is obtained. The detailed derivation process of predictor composed of matrix and vector can be calculated analytically [11, 19]. Specific technical issues such as hyper-parameters tuning and model fitting procedures are investigated in [20-22].

$$Y(x) = \beta_0 \hat{y}_{lf} + Z(x) \xrightarrow{predictor} \hat{y}(x) = \beta_0 \hat{y}_{lf}(x) + r^T(x) R^{-1}(y_S - \beta_0 F) \tag{13}$$

Equation (13) is HK model for high-fidelity function. As shown in this equation, low-fidelity Kriging function multiplicatively scaled by β_0 is used as global trend function. β_0 indicates how much the low and high fidelity functions are correlated. Similar to the low-fidelity Kriging, $Z(x)$ is stationary random process which has 0 mean and covariance of $COV[Z(x), Z(x')] = \sigma^2 R(x, x')$. σ^2 is the process variance of $Z(x)$ and $R(x, x')$ is the spatial correlation function defined as $R(x, x') = \sum_{h=1}^{K} \theta_h \left| x_h - x'_h \right|^2$ (Gaussian exponential function). The BLUP in the right hand side expression is formulated by following the same steps with that of low-fidelity Kriging model and reader can refer to [11, 19] for details of constructing Kriging.

Defining the R matrix step is called model fitting procedure, which equals seeking hyper-parameter, θ_h. In model fitting procedure, hyper-parameter is sought by using maximum likelihood estimation (MLE) defined as Eq. (11). Equation (11) only depends on the hyper-parameter (θ_h) after substituting β_0 and σ^2 into the Eq. (11) because β_0 only depends on θ_h and σ^2 depends on θ_h, β_0. After taking logarithm, θ_h maximizing the likelihood function is determined implicitly by the numerical optimization. Equation (12) expresses the hyper-parameter of θ_h.

$$L(\beta_0, \sigma^2, \theta_h) = \frac{1}{\sqrt{(2\pi\sigma^2)^n |R|}} \exp\left(-\frac{1}{2} \frac{(y_S - \beta_0 F)^T R^{-1} (y_S - \beta_0 F)^T}{\sigma^2} \right) \tag{11}$$

Where, $\beta_0 = (F^T R_{lf}^{-1} F)^{-1} F^T R^{-1} y_S$, $\sigma^2 = \frac{1}{n} (y_S - \beta_0 F)^T R^{-1} (y_S - \beta_0 F)^T$

$$\theta_h = \arg \max_{\theta_h} \{ \ln[L(\theta_h)] \} \tag{12}$$

The efficient global optimization (EGO) algorithm is coupled with the HK model. As a first step towards optimization, 100 initial samples, evenly distributed, are selected by the optimal latin hypercube sampling (OLHS) for the design of experiment (DoE). The specific number 100 is determined from preceding studies [23, 24]. These studies show that when designer uses the OLHS method, reliable results can be obtained by using more samples than the number of design variables multiplied by 10. To obtain more reliable results, supplementing the additional inter-point samples between each design variable is recommended. Based on this, the present study involving the 9 design variables designates 100 as the number of initial samples.

After DoE using OLHS, HK model is constructed. With the computed results of 100 initial samples, Kriging for the low-fidelity function is constructed. The fidelity type of VFM is set to be density of mesh in this step. In Sequence, the refinement process is conducted. For the refinement process, Expected Improvement (EI) method [24] expressed as Eq. (16) is applied.

$$E[I] = (f_{\min} - \hat{y})\Phi\left(\frac{f_{\min} - \hat{y}}{s}\right) + s\varphi\left(\frac{f_{\min} - \hat{y}}{s}\right) \tag{16}$$

EI is a criterion that can improve the accuracy of the optimal solution and reduce the uncertainty of surrogate model simultaneously. 3 samples which maximize the EI value are added into the previous dataset. Additionally, there is an issue for using EI—stopping criteria. There are many kinds of stopping criteria related to EI such as k-sla rule [25], maximum iteration, N samples within tolerance percent of the last optimum

[26], maximum EI [24], etc. In this study, 5-sla rule is selected, which calls for stopping the sampling process when the current value is not better than the best-calculated value 5 times in a row. After finishing the refinement of the low-fidelity Kriging, the same procedures, such as DoE and constructing HK model for high-fidelity function, are conducted. At the final step, the optimal solution is sought using GA. All above optimization procedures are depicted in following flow chart, Fig. 5.

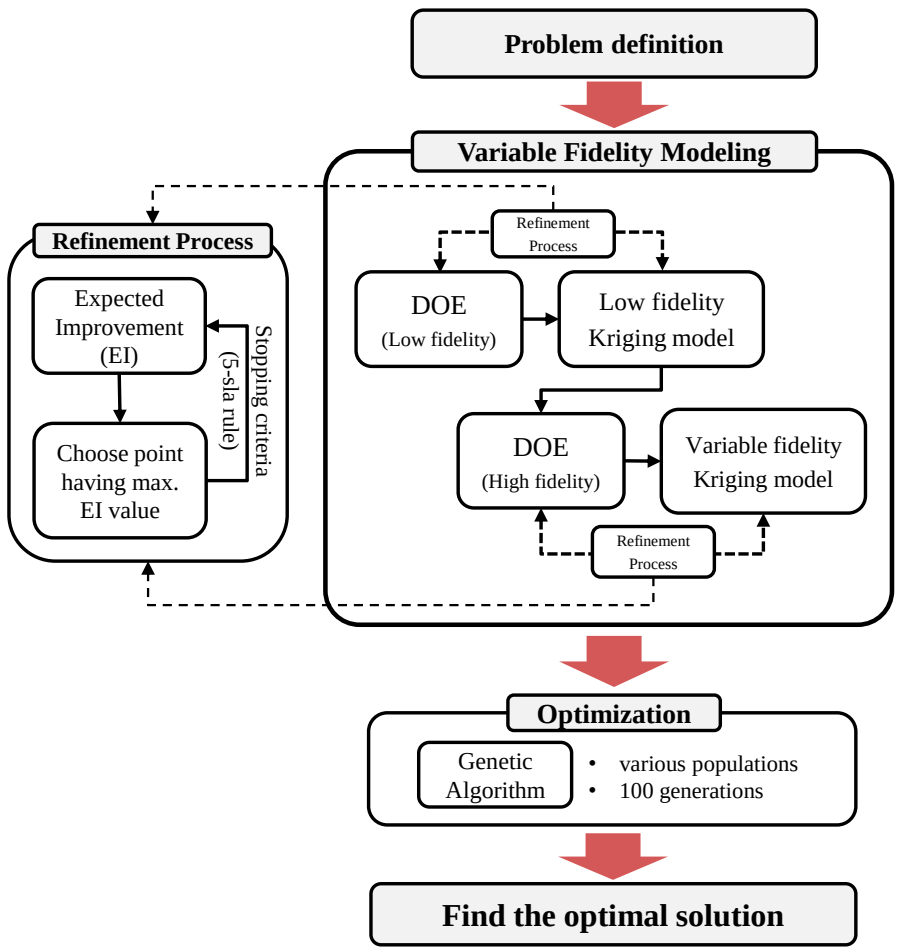

Fig. 5 Efficient Global Optimization (EGO) flow chart

D. Simplified and Fully Cooled Nozzle

Adiabatic analysis-based optimization is conducted with 2-level HK model constructed in different mesh densities with the same geometry. Specifically, the adiabatic analysis-based optimization uses simplified nozzle based on the fact that laterally averaged adiabatic wall temperature has consistent value [7] as in Fig. 6. In the simplified nozzle geometry, inner cooling components are eliminated except 3 hole arrangements as illustrated in Fig. 7. It is due to the fact that the nozzle surface temperature is only affected by the coolant extracted from the film cooling holes under the adiabatic condition, which means that the conduction effect generated from the inner cooling passage is not considered, and the contact area of the coolant and nozzle surface is the most critical factor in adiabatic analysis. It also helps to reduce the calculation time.

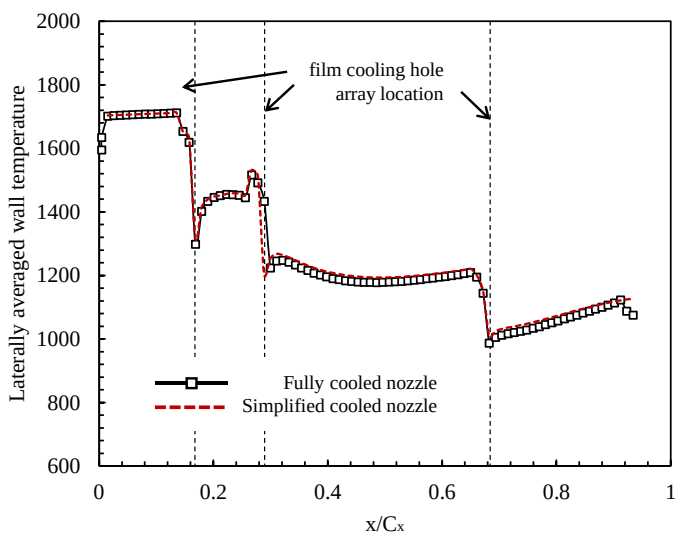

Fig. 6 Comparison of the laterally averaged adiabatic wall temperature between the fully cooled nozzle and the simplified cooled nozzles [7]

CHT-based optimization is conducted with 3-level HK model consisting of 2-level adiabatic analysis-based HK model and additional higher fidelity information obtained from CHT analysis for the third level of model. The number of higher fidelity initial samples is determined based on the number of the best case in adiabatic analysis-based optimization. Additionally, the same dataset is applied to construct the 2 lower levels of HK model. When it comes to geometry, CHT-based optimization uses the fully cooled nozzle contrary to the adiabatic analysis. The fully cooled nozzle contains all the inner cooling components such as rib turbulators, impinging holes, and leading edge film cooling holes, etc. as described in Fig. 7. These inner cooling components change the 3-D flow pattern of inner coolant, which plays the important role in cooling nozzle. For instance, recirculation zone generated behind the blade keeps the surface temperature low and when the large recirculation zone is formed by active interactions between coolant and inner cooling components, the surface temperature can be shown to be lower.

In summary, CHT-based optimization is executed using the already constructed 2-level HK model in adiabatic analysis-based optimization. On this HK model, the additional initial samples for construction of the third level of CHT HK model is added, whose number is determined based on the best high-to-low initial sample ratio in adiabatic analysis-based optimization. In other words, 2-level HK model is constructed with different densities under adiabatic condition and one more level of HK model is added using different solver fidelity; adiabatic and CHT analyses. Although the different nozzle geometries are adopted at the third level, it can be thought that all the levels in HK model are constructed with the information from the fully cooled nozzle based on the Fig. 6.

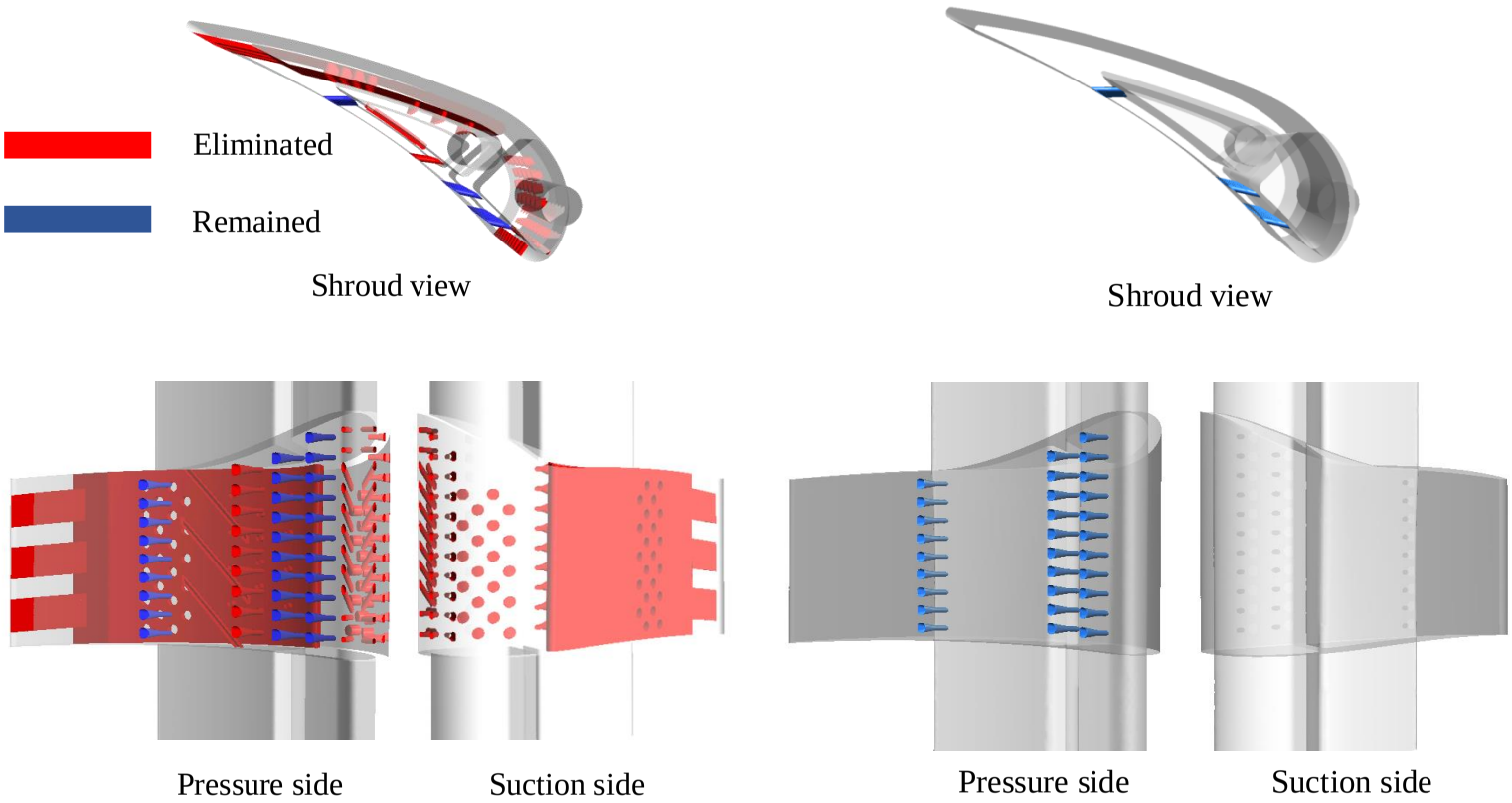

Fig. 7 Fully cooled nozzle and simplified nozzle geometries

E. Grid Topology

The present study uses two levels of grid systems for adiabatic analysis-based optimization and uses additional level of grid system for CHT optimization to provide various-fidelity information for VFM. In adiabatic analysis-based optimization, the low and high fidelity grid systems are composed of approximately 2 million and 8 million elements, respectively, as depicted in Fig. 8 and 9. The low-fidelity Kriging model is constructed with the coarse grid system. The information using the fine grid system is utilized to correct the low-fidelity Kriging model to the high-fidelity Kriging model. In addition, in regard to computation time, 2 million-grid takes about 40 minutes, and 8 million-grid takes 240 minutes per single calculation.

Figure 10 and 11 show the grids for CHT analysis, which are used as the highest level of HK model. The volume mesh is composed of approximately 30 million elements and solid mesh is composed of approximately 1.5 million elements. In addition, 2,000 minutes are required for the calculation of a single case, which is about 8 times longer than the adiabatic high-fidelity calculation. The third level of HK model is built with the calculated results using the CHT grid. The converged adiabatic 2-level HK model is regarded as the low-fidelity Kriging model in this step.

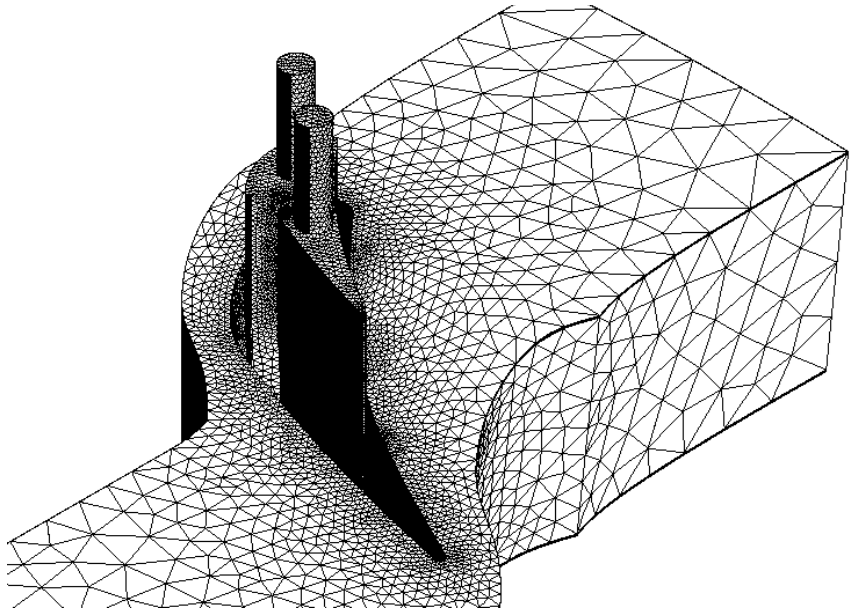

Fig. 8 Adiabatic low fidelity grid system

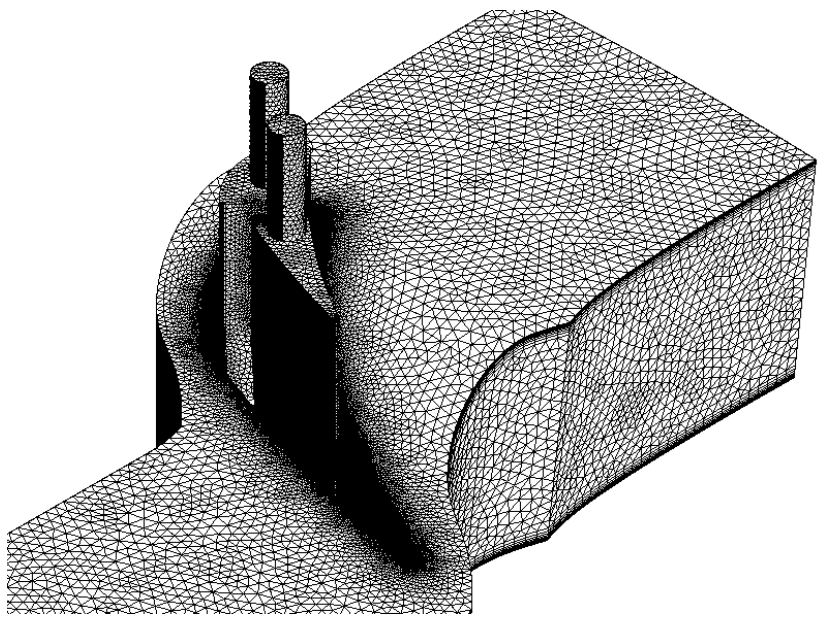

Fig. 9 Adiabatic high fidelity grid system

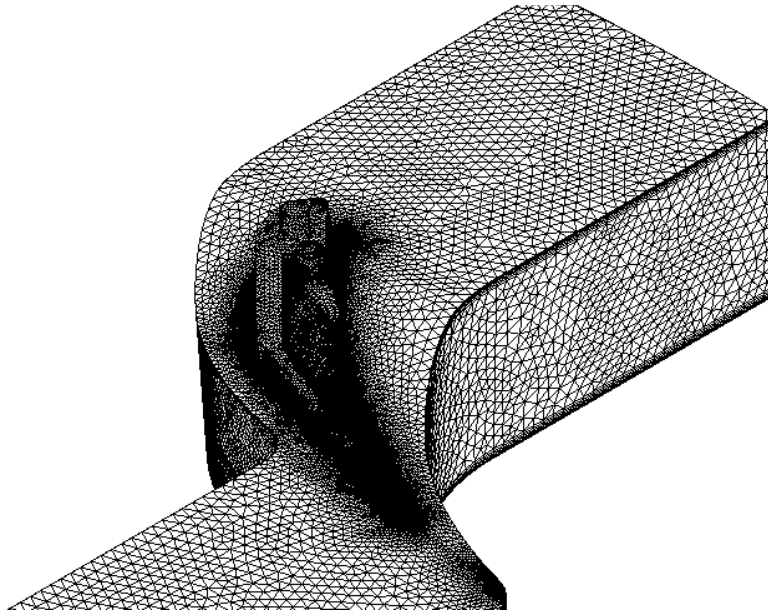

Fig. 10 CHT fluid domain grid system

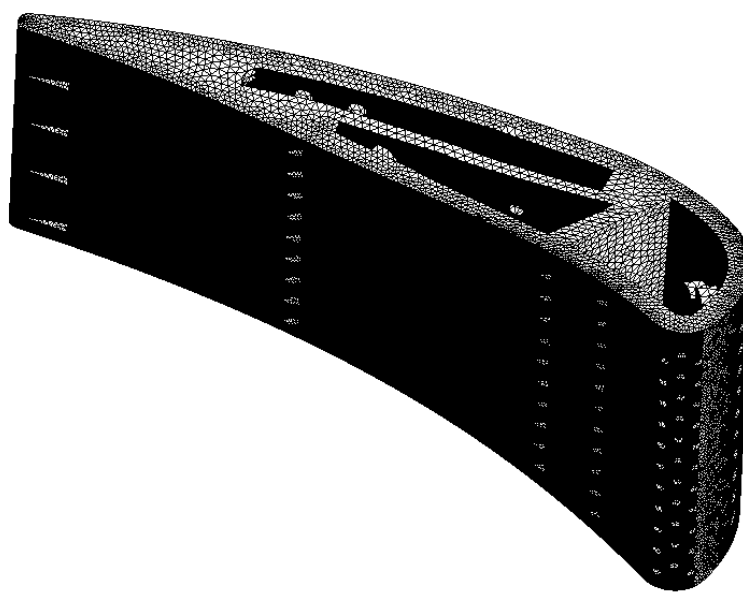

Fig. 11 CHT solid domain grid system

F. Grid Independent Test

For numerical accuracy, grid independent test is conducted. In adiabatic case, grid is tested in the range between 1 to 12 million-grid systems, as illustrated in Fig. 12. Grid independent test for CHT analysis is conducted in the range from 20 to 60 million-grid systems, as described in Fig. 13. The solutions calculated on different grids are plotted with abscissa, number of grid element. As shown in these graphs, the squared symbols have asymptotic property with increasing the number of grid element.

To show the grid independency more specific, the grid convergence index (GCI) is checked. This index is suggested for providing an objective asymptotic character while quantifying the uncertainty of grid convergence, which is based upon the theory of generalized Richardson Extrapolation. In other words, it is a measure of the percentage that the computed value is away from the value of the asymptotic numerical value. This index can be regarded as an error band. Therefore, the computation is accurate as GCI is getting smaller.

The GCI value is defined by Eq. (17). ε is relative error defined by difference of discrete solutions divided by finer grid solution and r is grid refinement ratio. p is the order of method and can be extracted directly from three grid solutions as defined by Eq. (18). In addition, F_s is called the safety factor whose value is usually chosen in the range from 1 to 3. However, usage of 1.25 is recommended for convergence studies with a minimum of three grids to confirm that the observed order of convergence p for the actual problem is reasonable. After obtaining GCI values on three grids, it is important to check that each grid yields solutions within the asymptotic range of convergence. Because exact solution, however, is not known in

many practical cases like the problem of this paper, the value defined by Eq. (19) is checked to verify the asymptotic range has been achieved. Close to 1 is regarded as the indication of good grid convergence. Detailed information of the GCI can be found in [27, 28].

$$GCI_{fine} = F_s \frac{|\varepsilon|}{r^p - 1} \tag{17}$$

$$p = \ln\left(\frac{f_3 - f_2}{f_2 - f_1}\right) / \ln(r) \tag{18}$$

$$\frac{GCI_{23}}{r^p GCI_{12}} \cong 1 \tag{19}$$

In this study, the value appears 0.982 at the adiabatic grid independent test and 1.02 at the CHT grid independent test. It can be said that grid systems utilized in this study sufficiently guarantee the grid convergence. Therefore, 8 million elements grid is adopted in adiabatic high-fidelity analysis and 31.5 million grid system is adopted in CHT analysis. Additionally, in Fig. 14, specific physical phenomena are detected on the pressure side of nozzle, the domain of optimization, in the cases using above 31.5 million grid system. In terms of film cooling coverage, distinct tail shapes are found on the pressure side as well as suction side.

Furthermore, numerical calculations continue until satisfying the convergence criteria. In detail, mass of inlet and outlet, momentum flux reach a steady state. In addition, to satisfy the global conservation for all transport equations, the imbalances of momentum, mass, and energy are checked and become less than 10^{-3} %. Root-mean-square (RMS) residuals of those also become less than 10^{-4}.

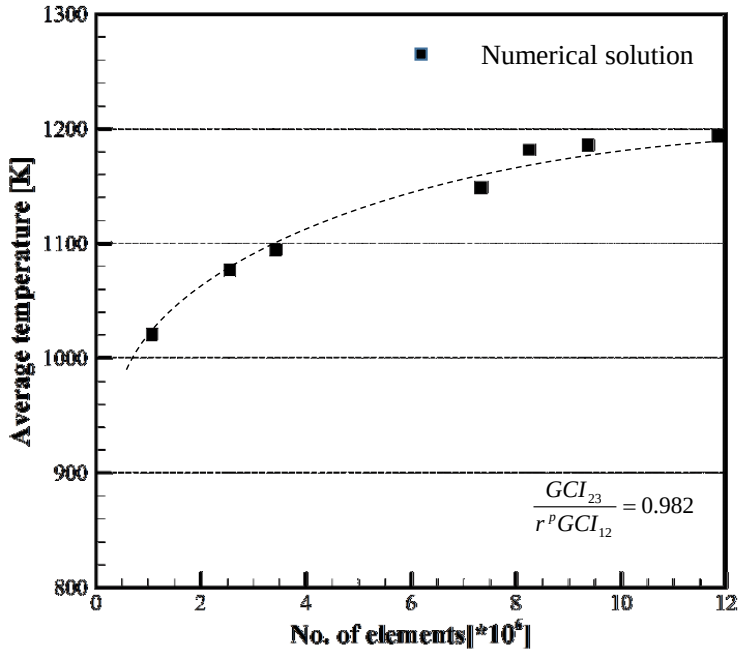

Fig. 12 Grid test results in number of elements

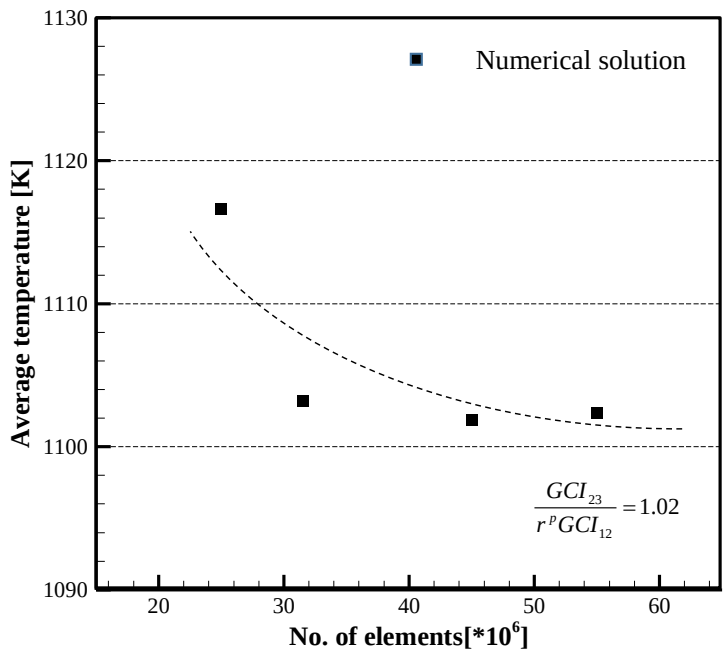

Fig. 13 Grid test results in number of elements

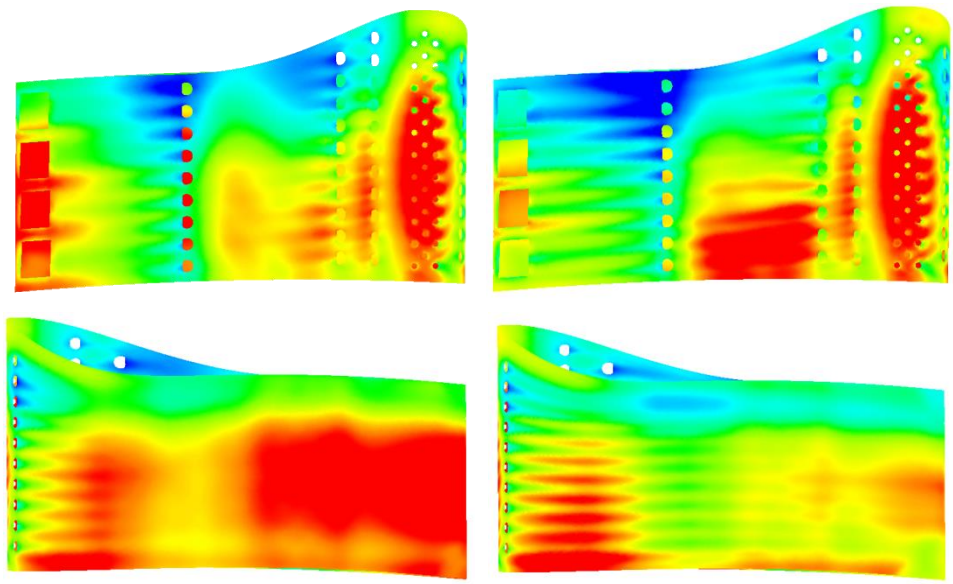

a) CHT result of 25 mil. elements **b) CHT result of 31.5 mil. elements**

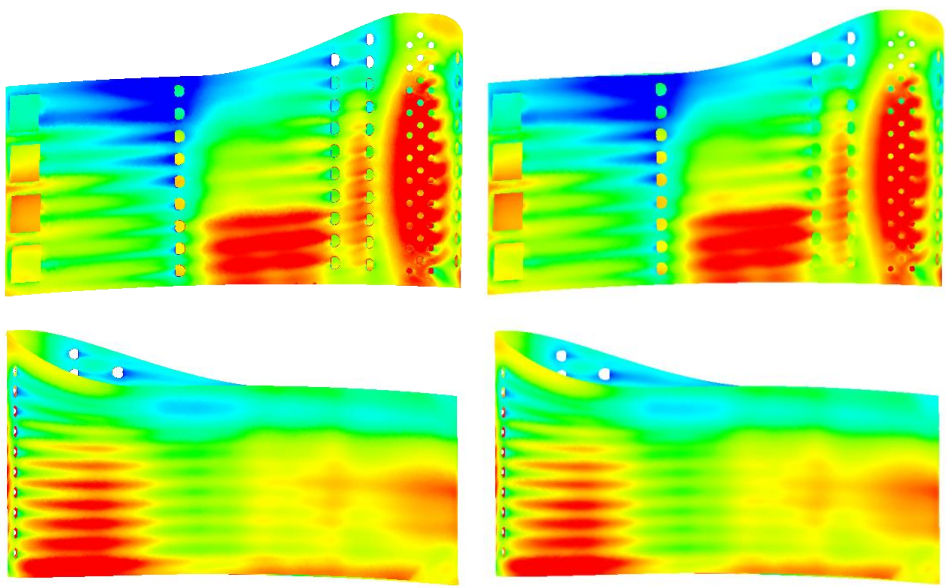

c) CHT result of 45 mil. elements **d) CHT result of 55 mil. elements**

Fig. 14 CHT grid independent test results

III. Results and Discussions

A. Ambiguity-clarifications of HK Model[29]

In this chapter, the computation time and optimized geometries of the film cooling hole array are presented by dividing the cases based on the number of high-fidelity samples. With these results, the existence of an optimal high-to-low fidelity sample ratio is proved, and the HK model's reliability of yielding similar converged solutions is also validated.

Table 3 Number of initial samples for VFM

	No. of Initial samples	
Fidelity	**Low**	**High**
Case0	-	100
Case1	100	2
Case2	100	10
Case3	100	20

Table 3 shows the combinations of the number of initial samples for the adiabatic analysis-based optimization, where the combinations are classified into 4 cases. Prior to the investigations of the optimization results, the reference case should be necessary for comparative analyses. Since the experiment of HPT, however, is extremely time-consuming and expensive, it is difficult to obtain the experimental optimization result in this problem. Thus, Case 0 which uses 100 high-fidelity samples only is set to be the reference case. This case can be regarded as a semi-exact solution in this study.

Table 3 is the results of adiabatic VFM. As mentioned above, Case 0 is reference case which is the optimization case with high-fidelity only. Case 1, Case 2, and Case 3 are VFM cases under the adiabatic condition. For the low-fidelity Kriging construction, the evenly distributed 100 low-fidelity samples are extracted, and refinement process is conducted with the same criterion as Case 0. The only difference between the 3 cases is the number of initial samples. To be more specific, Case 1 selects only 2 initial points—the optimal point of converged low-fidelity model and the arbitrary point around the optimal point. Case 2 selects 10 initial samples, and Case 3 employs 20 initial samples based on the OLHS. As mentioned before, from the results of these cases, it would be further investigated whether a best ratio of high- and low-fidelity samples with respect to computation time reduction exists and whether each HK model yields similar converged solutions regardless of the high-to-low initial sample ratio. Additionally, the computational cost and the optimized geometries of film cooling hole array will be discussed.

Table 4 Number of samples for adiabatic analysis-based optimization

No. of samples	Case 0	Case 1	Case 2	Case 3
LF initial	n/a	100 with OLHS method (3 cases mesh error)		
No. of Refinements	n/a	8	8	8
LF total	n/a	121	121	121
HF DoE method	OLHS	The best 2 points	OLHS	OLHS
HF initial	100 (6 cases mesh error)	2	10	20
No. of Refinements	15	20	17	13
HF total	139	62	61	59
CPU Time [min]	33360	19720 (-40.89%)	19480 (-41.61%)	19000 (-43.05%)
Averaged Temperature [K]	1066.49	1070.34 (+0.36%)	1059.35 (-0.67%)	1063.36 (-0.29%)

i. Computational Cost

The computation is conducted on 10 cores using an Intel i7-4930K CPU. All of the detailed results are summarized in Table 4. Case 0 uses totally 139 high-fidelity samples. More specifically, the Kriging model is constructed by evenly distributed 100 initial samples selected using the OLHS and 15 refinements are conducted for satisfying the stopping criterion. At each step, 3 samples which maximize the EI value. As a result, Case 0 takes 33,360 minutes of CPU time are added.

Case 1, Case 2, and Case 3 are the cases of the 2-level VFM. First, to construct the low-fidelity model, 100 initial sample points are extracted using the OLHS and 8 refinements are conducted. Consequently, 121 samples are utilized in total. With this converged low-fidelity Kriging model, Case 1 selects the 2 initial points from the low-fidelity model for modeling the HK model. These 2 points are re-calculated using the high-fidelity grid system for the high-fidelity initial samples. Then, EI refinements are repeated 20 times. Figure 15 summarizes the results of the CPU time reduction compared to the reference case and average temperature of the optimized turbine nozzle pressure side. The total CPU time of Case 1 is 19,720 minutes, which amounts to a 40.89% time reduction compared to the reference case. Next, Case 2 refines 17 times with 10 high-fidelity initial samples. The total CPU time is 19,480 minutes, which corresponds to a 41.61% time reduction. Finally, Case 3 is the VFM case with 20 high-fidelity samples also selected by the OLHS. 13 refinements are conducted and 19,000 minutes of CPU time are required, which is a 43.05% time reduction compared to the reference case. As the number of initial samples increases, the time

reduction slightly increases. These results, however, mean that the CPU time reduction has a similar level. Nevertheless, regarding the average temperature of the optimized turbine, the lowest averaged temperature, 1059.35 K, is turned up in the VFM case with 10 high-fidelity samples. Exceptionally, the VFM case with 2 samples has a higher temperature than the reference case. It can be concluded that selecting 2 high initial samples cannot afford to search for the right optimal point effectively.

In summary, when applying the HK model to construct the surrogate model, the time of the optimization process is reduced by -40.89% in Case 1, -41.61% in Case 2, and -43.05% in Case 3 compared to the high-fidelity only optimization. Based on these results, the best ratio of high-to-low fidelity samples does not exist—there is a less than 2.16% difference in time reduction. On the other hand, comparing the results of the objective function, Case 1 has 1070.34 K, Case 2 has 1059.35 K, and Case 3 has 1063.36 K. Case 2, which also has few differences—less than 0.67%, is the best case from the perspective of minimizing the average surface temperature of the nozzle pressure side. Because this result satisfies the purpose of the optimization, the combination of Case 2 can be thought to guarantee the better solution close to the exact real solution.

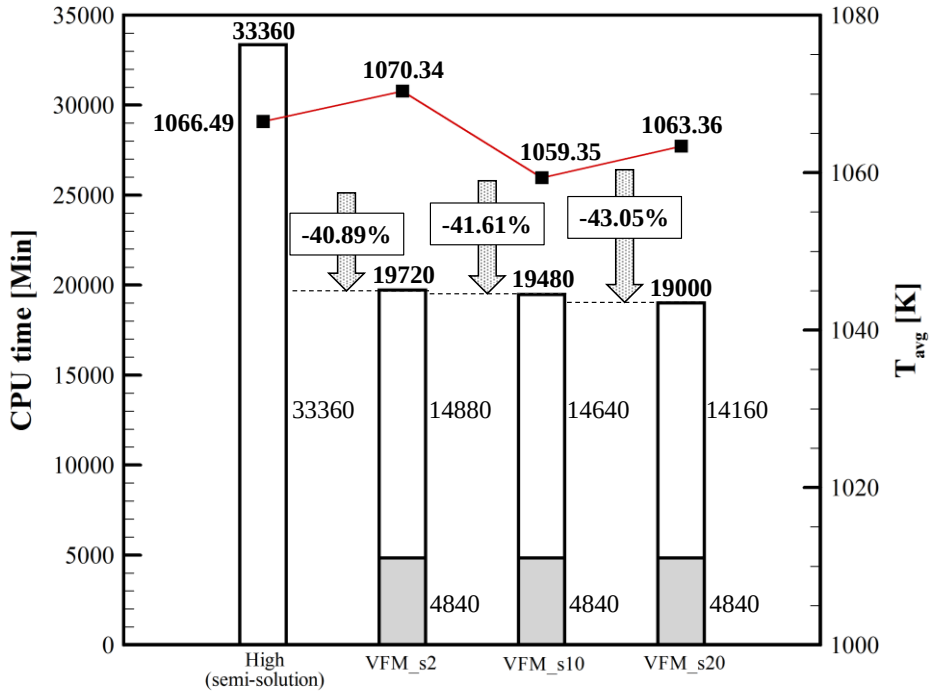

Fig. 15 Computational cost of adiabatic analysis-based optimization

ii. Resultant Geometries of Optimization

The resultant geometries of optimization are depicted in Fig. 16. Figure 16 (a) is the optimization result of the reference case, Case 0, which can be the baseline for comparison. Investigating the reference case first, as illustrated in Fig. 16 (a), the location of ROW0 is fixed at the front of the "pressure side", where the domain is defined in Chapter Ⅱ.B. Additionally, it is already shown that the array of ROW1 is moved to ROW0 as close as possible and that all holes of ROW1 are located between each hole of ROW0. In the adiabatic condition, curtailing the area between ROW0 and ROW1 is significant to reduce the average surface temperature because this area is directly exposed to the inlet gas with a high temperature. Therefore, the closer ROW0 and ROW1 are, the lower the average surface temperature is. In addition, positioning each hole of ROW1 perfectly between each hole of ROW0 can lead to reducing the area, so the average surface temperature decreases.

Looking at the optimized geometries with reference to the discussions of Case 0, similar geometries have been obtained in all the optimized cases. Following Fig. 16 (b), (c), and (d), the array of ROW1 also attempts to be moved toward the nearest location around ROW0. In addition, all holes of ROW1 are also located between the spaces of the holes of ROW0. Among the optimized cases, the holes of Case 2 and Case 3 are more perfectly located at the ideal place. As a result, the lower average surface temperatures appear in comparison with the reference case. Especially, Case 2 is the best case. At last, although the tendencies of the ROW2 array are slightly different in each case, they have two things in common: one is that the array tends to migrate in the upstream direction, same as ROW1, and the other is that the holes of ROW2 are slightly biased towards the hub. When examining the temperature contours,

the noticeable differences brought from ROW2 are not discovered. Based on the above results, even though the HK models constructed with different numbers of high-fidelity initial samples are used in the turbine optimization, similar geometries are obtained. It means that the HK model can yield reliable results irrespective of the number of high-fidelity initial samples.

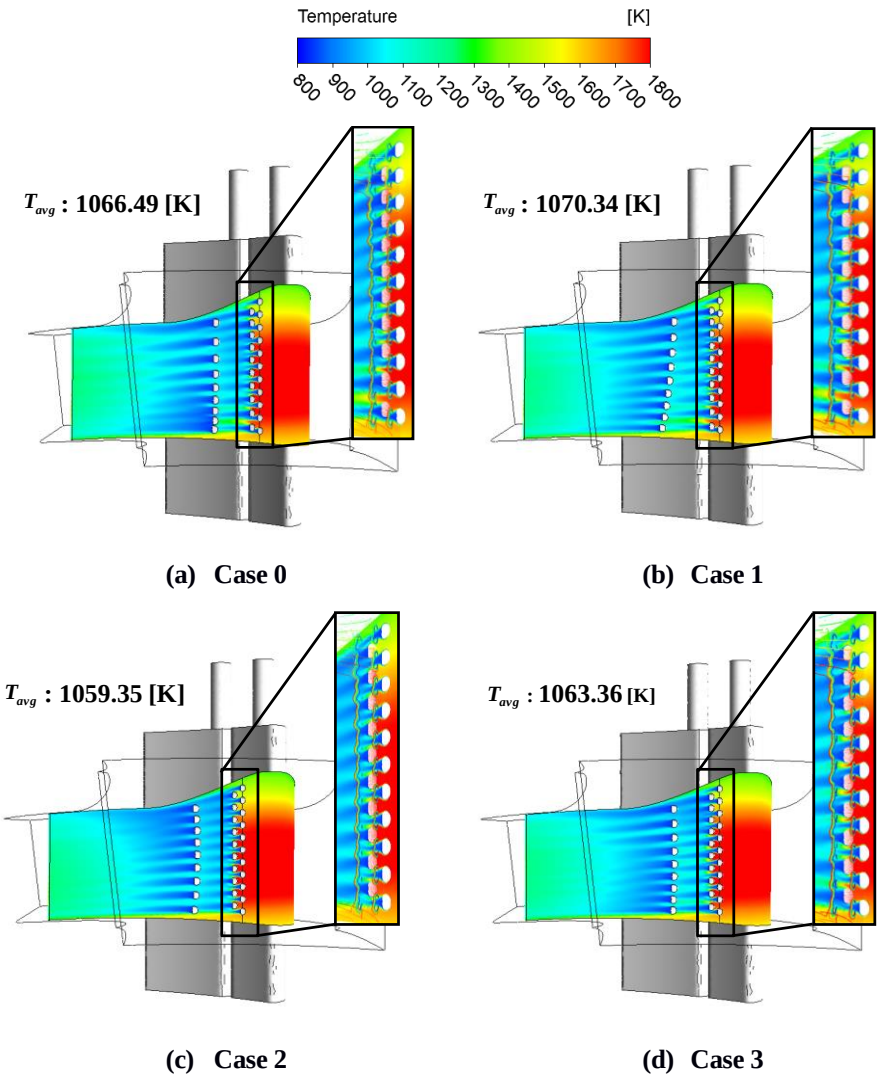

Fig. 16 Resultant geometries of optimization

B. CHT Optimization Results

CHT-based optimization is conducted within the same optimization framework of adiabatic analysis-based optimization. Since the best case, Case 2, of adiabatic analysis-based optimization used 10 high-fidelity initial samples, the same number of initial samples is selected by using the optimal latin hypercube sampling (OLHS) method in the design space.

The overall results are summarized in Table 5. With 10 initial samples extracted by OLHS, 3-level HK model is constructed on the already constructed adiabatic 2-level HK model. In other words, the HK model of Case 2 is used as the low fidelity Kriging model and construction process of HK model is additionally executed with the 10 highest fidelity initial samples including 5 refinements. As a result, 205 samples are used to construct 3-level HK model in total. Additionally, stopping refinement process at the 5th refinement means that the optimal value is discovered at the first refinement; no lower average temperature case appears during 5 times of refinements in a row.

Regarding the CPU time, as mentioned before in Chapter II. E, single CHT analysis takes about 2,000 minutes, which is approximately 8 times longer compared to the adiabatic high fidelity analysis. The total CPU time until obtaining the optimization result takes 65,480 minutes as shown in Table 5. In addition, the objective function, average surface temperature of nozzle pressure side, appears in 1,050.77K.

Table 5 Number of samples for CHT-based optimization

<table>
<tr><th>Level of HK model</th><th colspan="3">Number of samples</th></tr>
<tr><td rowspan="4">Level 1-2
2-level adiabatic HK model
(Adiabatic analysis-based
optimization result [8])</td><td></td><td>Level 1</td><td>Level 2</td></tr>
<tr><td>Initial</td><td>100
(3 mesh errors)</td><td>10</td></tr>
<tr><td>Additional
(refinement)</td><td>24(8)</td><td>51(17)</td></tr>
<tr><td>Total</td><td colspan="2">182</td></tr>
<tr><td rowspan="3">Level 3</td><td>Initial</td><td colspan="2">10
(2 mesh errors)</td></tr>
<tr><td>Additional
(refinement)</td><td colspan="2">15(5)</td></tr>
<tr><td>Total</td><td colspan="2">23</td></tr>
<tr><td>CPU Time [min]</td><td colspan="3">65,480</td></tr>
<tr><td>Average Temperature [K]</td><td colspan="3">1,050.77</td></tr>
</table>

i. Computational Cost and Convergence History

Computational cost should be compared between the total time of variable fidelity optimization and that of high-fidelity only optimization. In CHT-based optimization, the high-fidelity only optimization indicates optimization of CHT analysis only. However, because it is too time-consuming and practically unaffordable work, the estimated value is utilized as the total CPU time of high-fidelity only optimization. More in detail, the computation time of high-fidelity only optimization is estimated by using the same number of samples in the adiabatic reference case, Case 0, in which 139 samples are used to construct converged Kriging model in total. In consequence, 278,000 minutes of total CPU time is obtained from multiplication of 139 samples and 2,000 minutes in single CHT analysis, which is depicted in Fig. 17.

In the 3-level HK model optimization case, since the HK model of level 1 and 2 is just brought and used from the adiabatic analysis-based optimization, the CPU time of the first and second level is equivalent to that of the best case in adiabatic analysis-based optimization, Case 2. The CPU time of the third level is calculated with the 8 initial samples and additional samples in refinement process. As shown in Table 5, 23 samples are used until the convergence of 3-level HK model in total. As a result, 65,480 minutes of the total CPU time is obtained and CPU time is reduced by approximately 76.45% as depicted in Fig. 17.

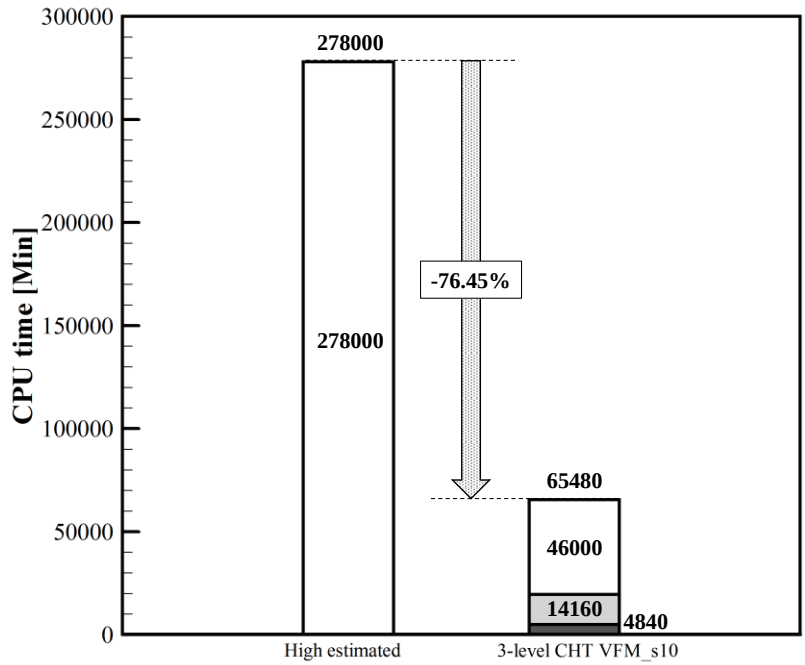

Fig. 17 CPU time of CHT-based optimization

Figure 18 illustrates the convergence history of all the cases including CHT-based optimization as well as adiabatic analysis-based optimization cases which has been conducted using 2-level HK model. The locations of the first point are determined by summing up the analyzing time of the initial samples. Since the numbers of high and low initial samples are different in each adiabatic case, the starting points of each graph are different as described in the graph. In CHT-based optimization, because additional initial samples to construct the 3-level HK model are used, the starting point of 3-level CHT VFM graph, expressed with round symbol, is determined by the sum of CPU time of CHT initial samples and that of VFM with 10-high fidelity samples—Case 2. In addition, the gap of the each symbol indicates the CPU time per

one refinement. It can be found that CHT refinement takes significantly more time compared to adiabatic refinement.

Finally, it can also be known in Fig. 18 that the gradient of each graph becomes steeper, as the number of initial samples is increasing. It means that when more initial samples are used, the HK model can converge to the solution faster. In addition, comparing the slope of the graph based on the level of HK model, 3-level HK model is seeking the optima faster than 2-lelvel HK model. It can be concluded that the convergence rate is better as the level is getting higher.

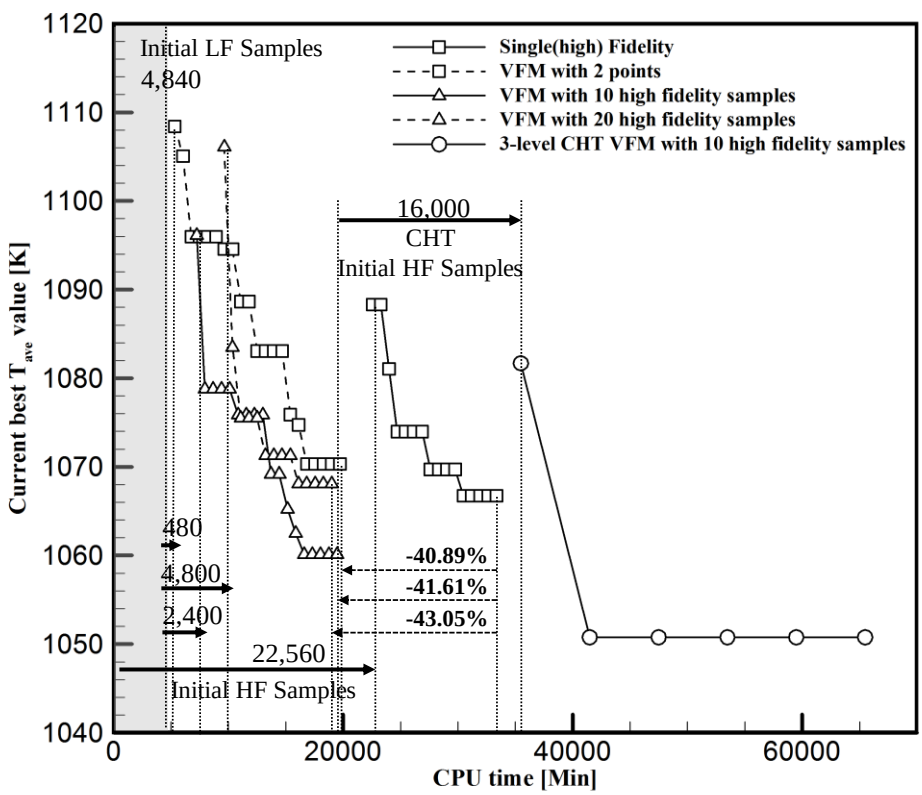

Fig. 18 Convergence history

ii. Resultant Geometry of Optimization

Figure 19 (a) indicates the baseline surface temperature contour on the pressure side using CHT analysis. In addition, the surface temperature distribution of CHT optimized nozzle is depicted in Fig. 19 (b). Regarding to the resultant hole arrangement, the optimized nozzle has straight second array, ROW1, located towards the ROW0 as close as possible. Moreover, all holes of ROW1 are positioned between the holes of ROW0, which is the same result of the adiabatic analysis-based optimization. On the other hand, the third array, ROW2, shows totally different hole arrangement; parabola shape with the vertex moved towards the upstream direction as possible in the design space of ROW2 and slightly biased towards the shroud direction.

When it comes to the objective function, average surface temperature decreases in the optimized geometry compared to the baseline. As shown in Fig. 19 (a) and (b), the average temperature of baseline is 1100.41 K and that of CHT optimized geometry is 1050.77 K. Consequently, 49.64 K of temperature reduction is obtained after the optimization. The temperature difference distribution subtracting temperature of CHT optimized nozzle from that of baseline is described in Fig. 19 (c). The blue region indicates the area representing CHT optimized nozzle has better cooling performance than baseline. As shown in Fig. 19 (c), although there are certain regions in the downstream showing surface temperature of CHT-based nozzle is slightly higher than that of baseline, significantly large decrease of temperature is derived in the broad domain of upstream. This leads the average temperature to be lower.

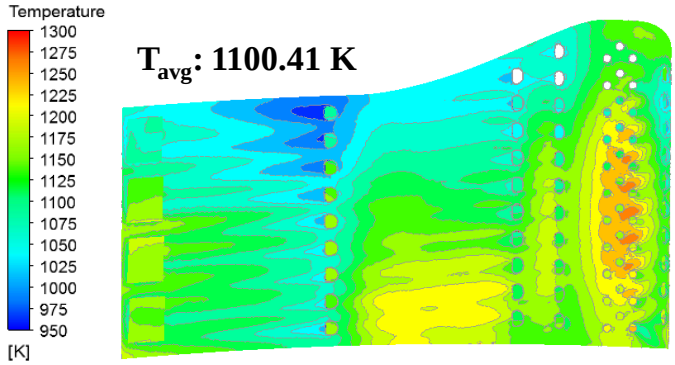

(a) Baseline temperature contour considering CHT

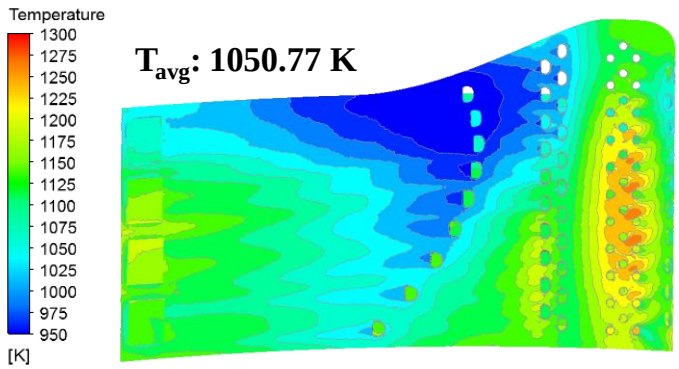

(b) Temperature contour of resultant geometry from CHT-based optimization

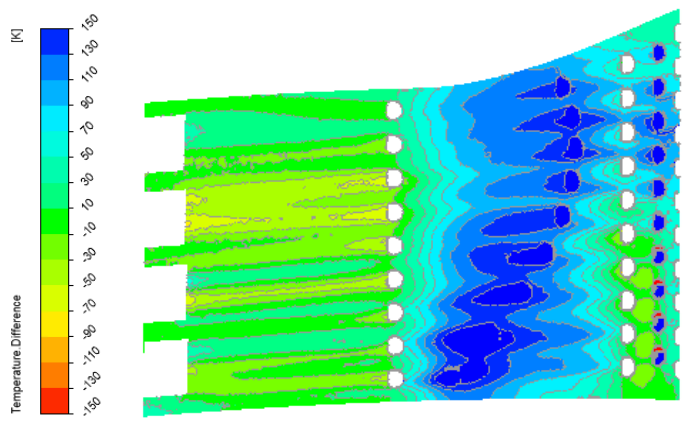

(c) Temperature difference contour of baseline and CHT optimized nozzle

Fig. 19 Temperature contours in CHT analysis

Analyzing the baseline temperature distributions in detail, it can be found that hub temperature appears higher than shroud, which comes from the geometry of target nozzle used in this study. Specifically, the pressure side of target nozzle has concave geometry and flow passage area decreases at the shroud. Because the concave geometry makes the film cooling flow pressed inwards, it leads the coolant extracted from the holes attached well on the nozzle surface and the flow accelerated, which are contradictory phenomena to the flat plate case. Moreover, since flow passage area decreases around the shroud, the effect of concave geometry in film cooling is more activated as mainstream goes by. As a result, relatively high temperature is generated at the hub and better film cooling performance appears at the shroud.

On the other hand, the reason why the shape of second hole array is determined can be known by analyzing the chord-wise temperature distribution. The temperature at the upstream region is high compared to the downstream. It is because the leading edge region is directly exposed to the inlet gas with high temperature, which is propagating to the upstream. From the perspective of reducing the surface average temperature, curtailing the area where hot stream from inlet gas is propagated is top priority. Therefore, the second hole arrangement attempts to move towards the nearest location at the first array after the optimization to reduce the area between the first and second hole arrays as found in Fig. 19 (b). In addition, the area is reduced effectively by the way all the holes of the second array are positioned between each hole of the first hole array.

The shape of the third hole array, however, is determined not by propagated high temperature but by the coolant flow pattern. The film cooling hole plays the role of making lower pressure region and extracting the coolant and accelerating the coolant

velocity around hole. Therefore, different hole arrangement causes different pressure distribution and also makes different flow pattern inside the inner cooling passage. Figure 20 shows the pressure and velocity contours including velocity vectors investigated at the wall of inner passage pressure side. Looking at the baseline velocity field in Fig. 20 (a), most of the coolant is directly pressed out into the holes flowing on the rib turbulators with little interaction with inner cooling components. While the flow pattern of baseline is relatively simple, optimized nozzle has generated complicated pressure distribution and flow pattern as described in Fig. 20 (b). In particular, recirculation is essential phenomenon in analyzing the inner flow pattern. Recirculation is stagnated coolant movement in circle with slow velocity, which is usually generated by the geometry such as rib-turbulators. The Low pressure produced by the film cooling hole also influences generation of recirculation as mentioned before. In the pressure contours of Fig. 20 (a) and (b), it can be found that pressure of the optimized nozzle is kept high compared to the baseline because there is only one hole under the first turbulator. In addition, when flow passes through the recirculation, recirculation makes flow velocity decelerated and pressure reduced. As a result, overall flow pattern is becoming entirely different.

Regarding the target model used in this study, recirculation made by geometry is found at the front of the first turbulator where low pressure region appears, which can be found precisely in the streamlines at the lowest dotted square of Fig. 20 (b). Especially between the second and third turbulators, it can be noticed that strong recirculation bubble is developed and the flow is splitting into opposite direction along the hole arrangement. As mentioned before, because the coolant flow is stuck and spins along the recirculation flow, coolant velocity in this area decreases. It also

induces the low pressure region to be developed. In addition, because coolant passing through the strong recirculation has low velocity, it is directly pressed into the impinging hole installed for suction side cooling, which can be found at the top dotted square in velocity contour of Fig. 20 (b). In terms of pressure, since the impinging hole ingurgitates the coolant, low pressure region is also developed around the impinging hole. Therefore, it can be found that low pressure region is developed at the coincident location of impinging hole in pressure contour of Fig. 20 (b). Moreover, a large recirculation bubble occurs in the upper side of the inner cooling passage due to the low pressure induced from impinging hole. The specific flow pattern at the upper side of inner passage is depicted in Fig. 21 with streamlines. It can be also known that coolant flowing down in large recirculation bubble reaches the holes located at the mid span and is utilized as the materials of the film cooling.

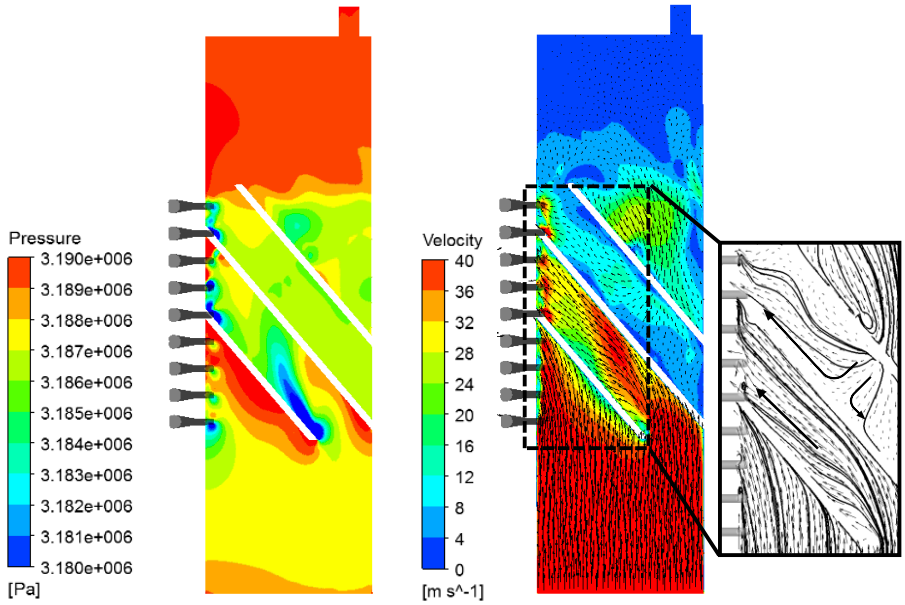

(a) Pressure (left) and velocity (right) contours of baseline

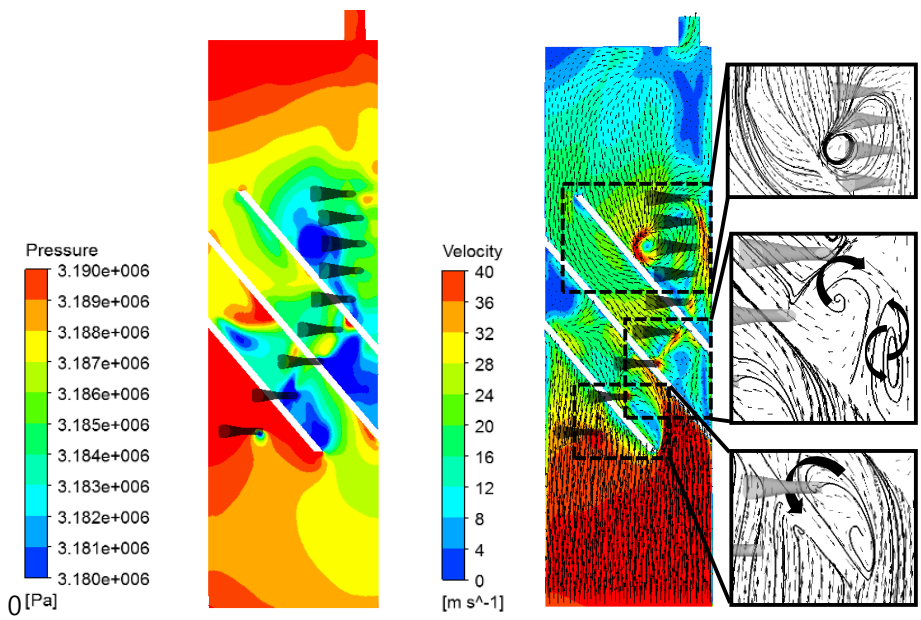

(b) Pressure (left) and velocity (right) contours of optimized nozzle

Fig. 20 Pressure and velocity contours of (a) baseline and (b) CHT optimized nozzle

To find the key factor of reducing the surface average temperature, the streamlines passing through the third film cooling hole array should be investigated. Because the coolant passing through holes of the third array is continuously provided from the inlet of inner cooling passage which comes from the compressor, temperature of coolant can be kept low. Coolant 3D flow pattern in the inner cooling passage of the baseline (a) and CHT optimized nozzle (b) is visualized in Fig. 21. The red lines indicate the streamlines passing through the three holes from the top and the green lines are the streamlines passing through the two holes from the bottom. The blue lines are the streamlines of the others.

To explain specifically, in the Fig. 21 (a), all the streamlines of baseline are sucked out to the holes flowing on the rib turbulators installed at the wall of inner cooling passage. In addition, the small circulation flow where red streamlines spin is generated around the mid span. In contrast, figure 21 (b) shows that streamlines of CHT optimized nozzle are being mixed in more complicated pattern than baseline. In detail, the red lines are extracted into the film holes with little interaction with rib turbulators; red streamlines are stuck for a short time in the recirculation bubble generated between the second and third turbulators. On the other hand, it can be found that blue streamlines are strongly influenced by both the film cooling holes and inner cooling components. In other words, recirculation is developed due to the active cooperation between rib-turbulators and film cooling holes. In consequence, as discussed before, it makes the flow especially between the second and third turbulators decelerated and the large recirculation developed at the upper side. Therefore, streamlines cover most region of inner cooing passage as shown in Fig. 21 (b). The down flow of

recirculation is also extracted through the film cooling hole. Additionally, the green streamlines seems to help the generation of large recirculation.

In summary, the shape of the third hole array is determined in the way of making the active recirculation developed at the upper side of the inner cooling passage. As a result, flowing down coolant keeping temperature low can reach the holes located at the mid span, so it is utilized as material of film cooling, which makes activity of taking heat away maximized. It can be verified that the low temperature region of nozzle pressure side, Fig. 19 (b), and streamlines passing through the film cooling holes, Fig. 21 (b), have a good agreement.

Additionally, Figure 22 represents the coolant mass flow rate of each hole in the second and third hole arrangements. In this figure, it can be confirmed that the amount of the coolant passing through the each hole is reduced after the optimization. Especially compared between baseline and CHT optimized nozzle, the mass flow rate at the second hole also decreases by 4.85 % as described in Fig. 22 (a). Furthermore, at the third hole arrangement, the mass flow rate of the coolant at the third hole array also significantly decreases by 28.69 %, from the 0.00292 kg/s to the 0.00208 kg/s, which can be found in Fig. 22 (b). The total mass flow rate of the coolant for film cooling is reduced by 12.76 %. This result means that the cooling performance has become better with using a little amount of coolant and it also lead the overall cycle efficiency of the gas turbine to be improved.

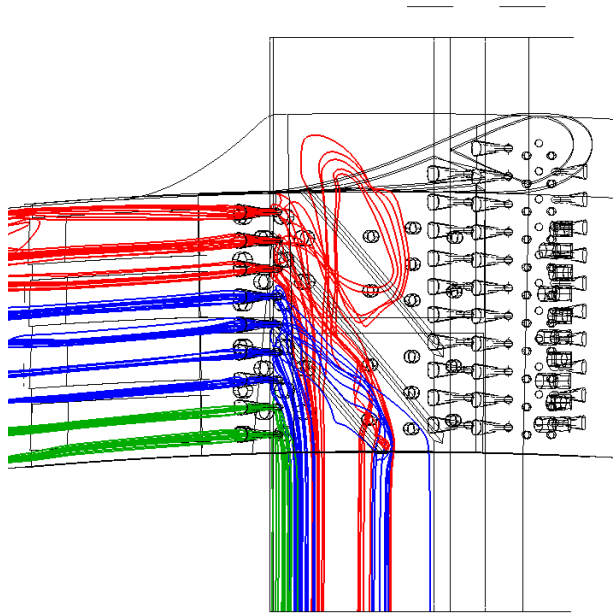

(a) Streamlines of baseline

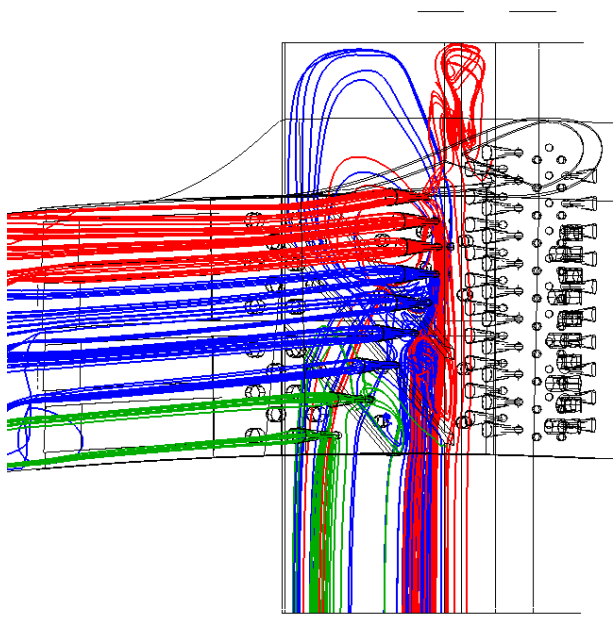

(b) Streamlines of CHT optimized geometry

Fig. 21 Streamlines of the (a) baseline and (b) CHT optimized geometry

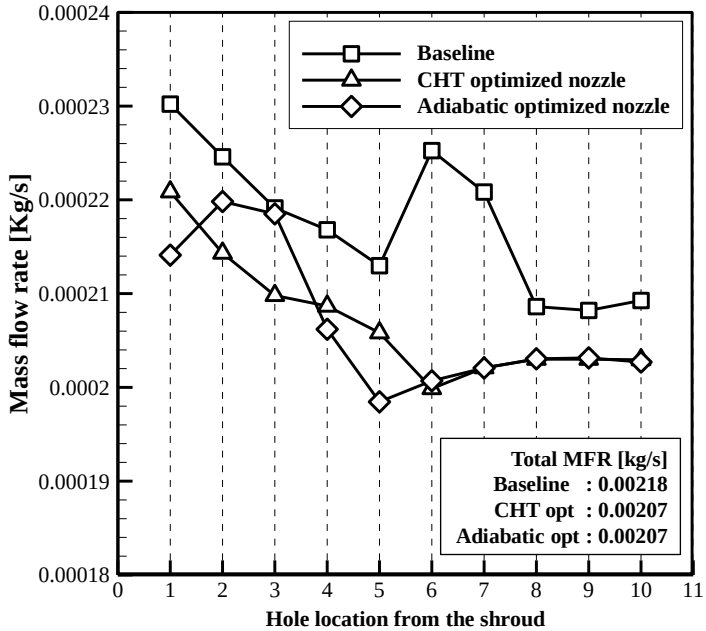

(a) Mass flow rate in the second hole array

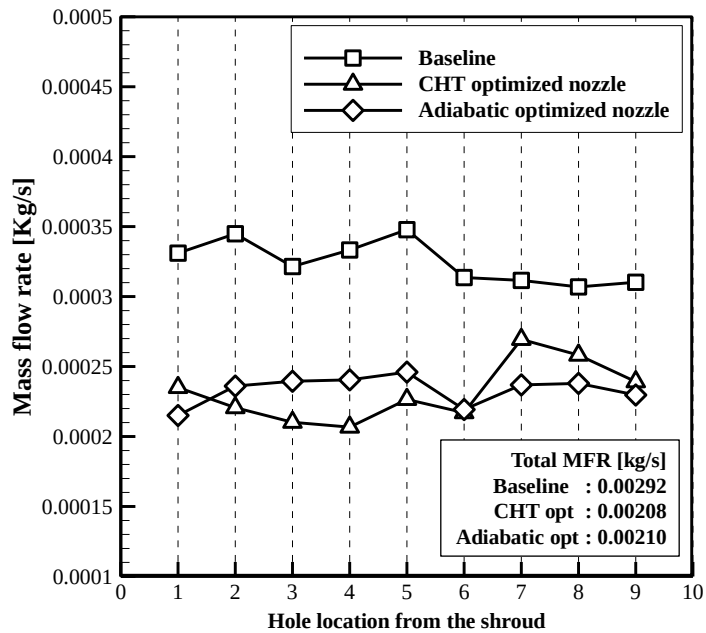

(a) Mass flow rate in the third hole array

Fig. 22 Mass flow rate of each hole in the (a) second and (b) third arrays

iii. Comparison between Results of Adiabatic and CHT-based Optimizations

Figure 23 is re-calculated temperature contour considering CHT applied with the resultant hole arrangement of adiabatic analysis-based optimization, Case2. Moreover, the fully cooled nozzle geometry which is equivalent to the model of CHT-based optimization is adopted. The average temperature appears in 1070.79 K as described in Fig. 23.

Compared to that of baseline, as illustrated in Fig. 19 (a), average temperature is reduced by 26.62 K. The detailed temperature difference distribution compared to the baseline is described in Fig. 24 (a). The blue field indicates area showing better cooling performance than baseline. Because the coolant extracted from the hole array moved towards the upstream is attached on the surface, the adiabatic optimized nozzle shows good cooling performance at the hub region limitedly where little amount of coolant cover in baseline. On the other hand, the adiabatic optimized nozzle has relatively higher average surface temperature than that of CHT optimized nozzle. Figure 24 (b) shows the detailed temperature difference distribution which is obtained by subtracting the CHT optimized nozzle result from the adiabatic result. The blue field in Fig. 24 (b) indicates CHT optimized nozzle has better cooling performance compared to the adiabatic optimized nozzle. Although the red region appears at the hub where no holes are located in CHT optimized nozzle, the area is too confined compared to the broad blue region that the result of CHT-based optimization has 20.02 K lower average temperature. In addition, it also matches the result that low temperature region is generated at the shroud in the resultant temperature distribution of CHT optimized nozzle.

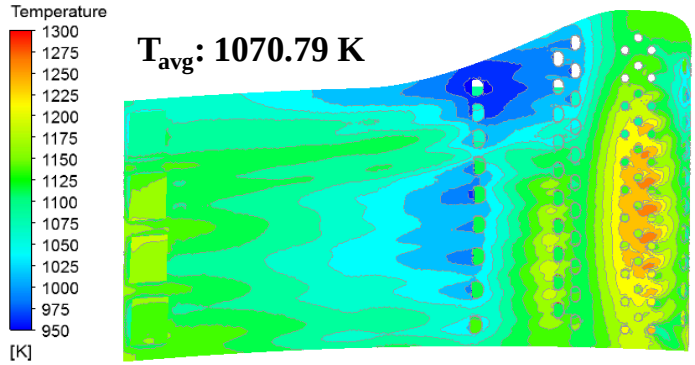

Fig. 23 Recalculated temperature of adiabatic optimized nozzle considering CHT

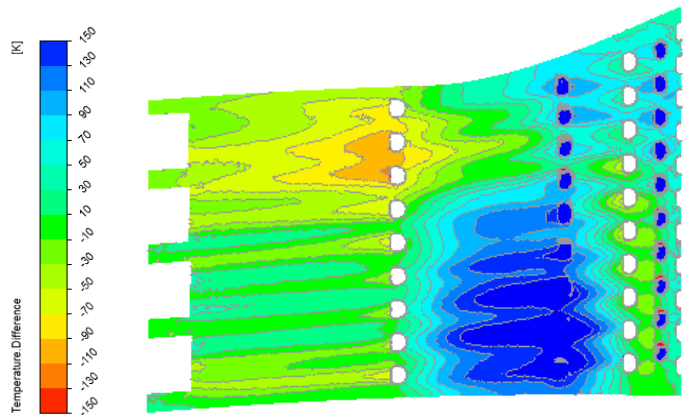

(a) Temperature difference contour of baseline and adiabatic optimized nozzle

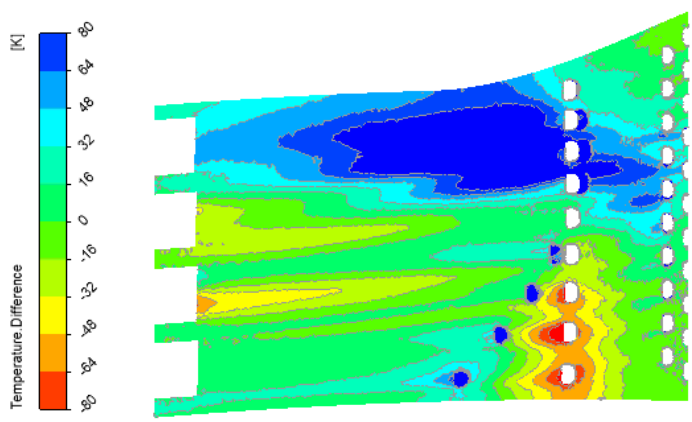

(b) Temperature difference contour of adiabatic and CHT optimized nozzle

Fig. 24 Temperature difference contours considering CHT

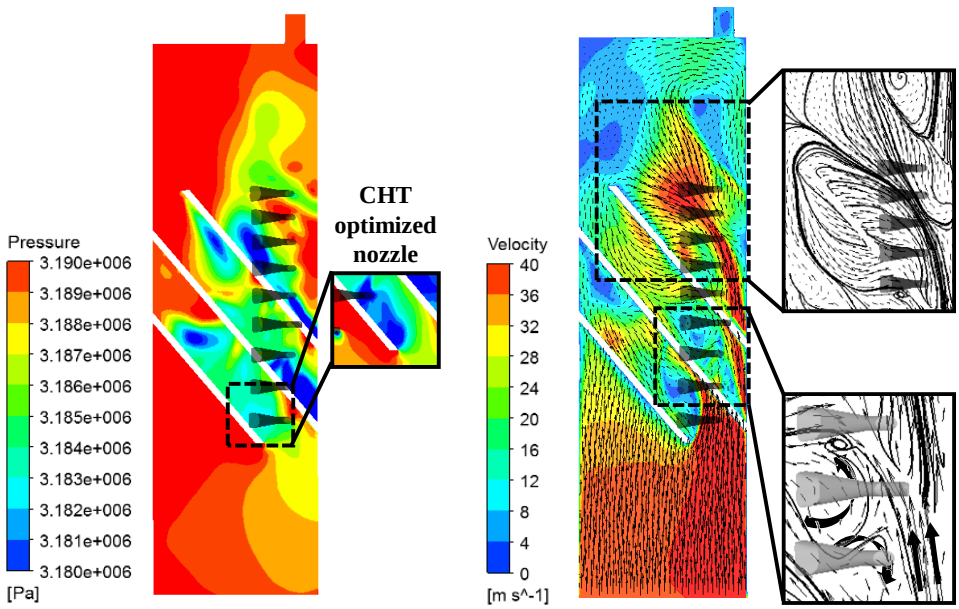

Fig. 25 Pressure and velocity contours of adiabatic optimized nozzle

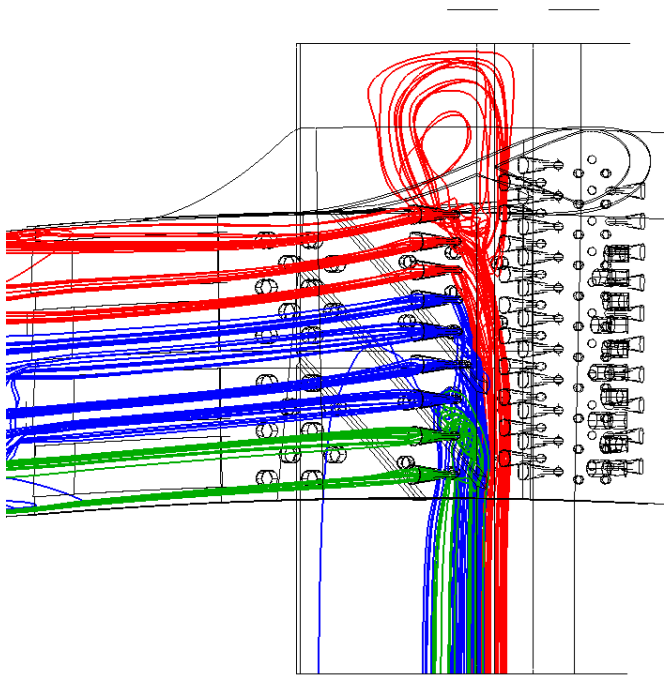

Fig. 26 Streamlines of adiabatic optimized nozzle

Figure 25 is pressure and velocity distributions at the pressure side of inner cooling passage in adiabatic optimized nozzle. The velocity contour includes velocity vector to investigate the flow pattern in detail. As discussed in previous section, the film cooling hole influences on generation of the low pressure region and various flow pattern in the inner cooling passage. In adiabatic optimized nozzle, since there is no hole below the first turbulator and all the film cooling holes are located at the front as possible in determined design space, the pressure of bottom is kept high compared to the other cases. Furthermore, the recirculation region, marked with dotted square in pressure contour where low pressure is contrastively turned up in CHT optimized nozzle, is diminished. It is because the lowest hole located at the front of the first turbulator extracts the coolant before recirculation flow is formed. In sequence, between the second and third turbulators in velocity contour, the holes located forward directly extract coolant as marked with dotted square in velocity contour. As a result, the formation of recirculation is disturbed and high speed flow appearing in red region is detected at this area; though, in CHT optimized nozzle, strong recirculation bubble is created and makes coolant velocity decelerated enough, so coolant directly pressed out into the impinging hole and a large circulation bubble is generated at the upper side of inner cooling passage. With the flow having large kinetic energy, flow is divided into two directions, as described in streamlines of Fig. 25. One is flowing up past the impinging hole and a small recirculation bubble is generated at the upper side. The other is flowing around the third turbulator. This turning flow is developed by the low pressure, which is induced by the effect of impinging hole. Additionally, because the downward coolant in the turning flow cannot reach the holes, it cannot be used as the material of film cooling, which can be found in Fig. 26. This result is contrary to the flow pattern in CHT optimized nozzle.

Figure 26 illustrates the streamlines passing through the third film cooling hole array. As mentioned before, because circulated flow around the third turbulator is generated and the coolant cannot reach the holes located in mid span, it can be found in Fig. 26 that only the coolant flowing up at the front is extracted to the film cooling holes Furthermore, the streamlines extracted at the top three holes—red lines—cannot be spread on the nozzle surface compared to the CHT optimized nozzle. In other words, the region filmed by the coolant extracted from the holes is relatively narrower than CHT optimization. Following the same discussion that coverage area of streamlines is closely related to the surface temperature distribution, good agreement is also investigated between Fig. 23 and 26. In consequence, the average surface temperature is turned up higher than CHT result.

When it comes to mass flow rate, although there exists slightly different tendency at the individual hole, the total mass flow rate passing through the second and third hole arrangements are almost same with those of CHT optimized nozzle, which is illustrated in Fig. 22. Therefore, it can be concluded that the overall efficiency of gas turbine with adiabatic optimized nozzle has similar value with that of CHT optimized turbine.

iv. Overall Film Cooing Effectiveness

The overall effectiveness of film cooling is assessed by the index called overall film cooling effectiveness (ϕ). The index is the non-dimensional metal temperature defined as Eq. (20) and also devised to take account into both convection and conduction effects simultaneously.

$$\varphi = \frac{T_\infty - T_W}{T_\infty - T_C} \tag{20}$$

T_∞ is inlet temperature of freestream. Because turbine is operated in transonic condition and inlet temperature has parabolic profile, it is difficult to specify the value of T_∞. Therefore, the adiabatic local surface temperature on nozzle without holes is calculated and adopted as T_∞. T_W is calculated surface temperature considering CHT and T_C is coolant inlet temperature, 837 K.

Figure 27 shows the overall film cooling effectiveness distributions of baseline (a), CHT (b), and adiabatic (c) optimized nozzles on the nozzle pressure side. As shown in these figures, baseline has 0.690 of average overall film cooling effectiveness, CHT optimized nozzle 0.748, adiabatic optimized nozzle 0.720. The CHT optimized nozzle has greater effectiveness than other two cases. Moreover, it can be found that high effectiveness region is evenly distributed on the pressure side. This reduces the possibility of generation of hot core, which is known as critical factor of the blade lifespan.

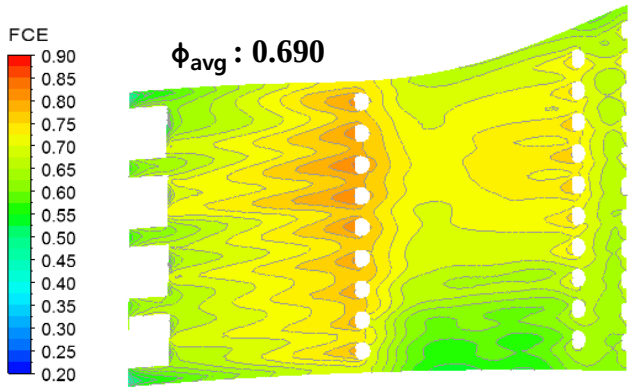

a) Baseline

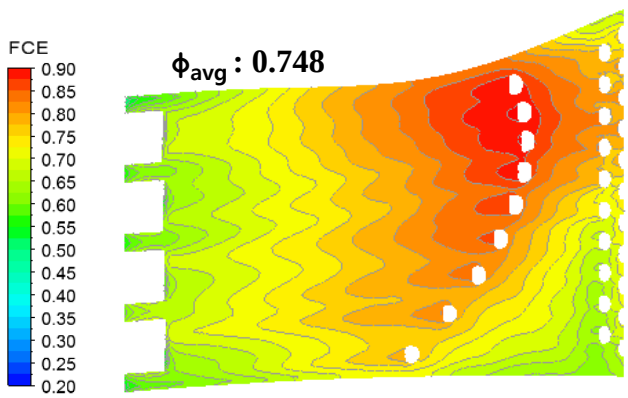

b) CHT optimized nozzle

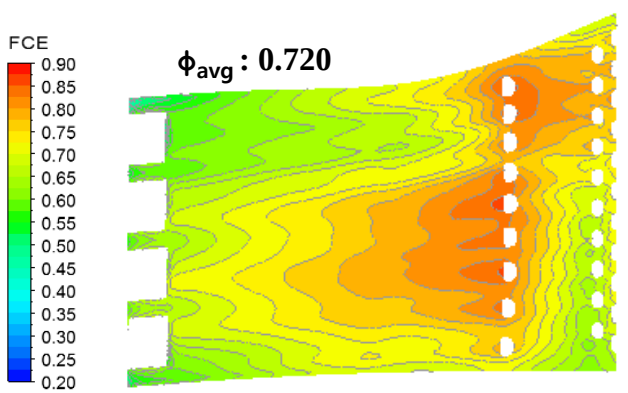

c) Adiabatic optimized nozzle

Fig. 27 Overall film cooling effectiveness contours on the nozzle pressure side

IV. Conclusions

This study aims to optimize the film cooling hole array on the nozzle guide vane of high pressure turbine (HPT) considering conjugate heat transfer (CHT) effects. For the optimization technique, efficient global optimization (EGO) algorithm coupled with the hierarchical Kriging (HK) model is employed to relieve the huge computation load in considering CHT. Prior to the CHT-based optimization, to efficiently utilize HK model in the film cooling hole array optimization, several ambiguities including high-to-low initial sample ratio, refinement criterion, and stopping criterion are clarified under the adiabatic condition as a preliminary study. In the adiabatic analysis-based optimization, the fidelity of the HK model is defined according to the mesh density and three cases of optimization are carried out with respect to different numbers of high fidelity initial samples. As a result, the CPU time required for overall optimization is significantly reduced by approximately 40%. Moreover, HK model can produce consistent and reliable results irrespective of initial sample ratio. Based on these results, 3-level HK model is constructed for CHT-based optimization. It is additionally constructed on the same dataset of 2-level HK model of the best case—Case 2—in adiabatic analysis-based optimization. All the optimization processes are same with the adiabatic analysis-based optimization. As a result, CHT-based optimization derives a quarter of overall CPU time. In addition, average surface temperature decreases by 49.64 K and totally different hole arrangement is obtained.

From above optimization series, the conclusions can be summarized as follows:

1) It is verified that HK model can not only produce the consistent and reliable result but also improve the calculation efficiency in the optimization conducted under the

adiabatic condition. More in detail, the difference of objective function, average surface temperature on the nozzle pressure side, is obtained under the 1% of error. The overall CPU time for optimization is reduced by approximately 40%. When it comes to hole array geometry, the similar hole arrangements are turned up irrespective of different high-to-low initial sample ratios, which is also similar to the result of the high-fidelity only optimization.

2) EI-based EGO algorithm coupled with HK model derives a quarter of CPU time in obtaining optimal configuration of hole arrangement compared to the estimated time of fully CHT analysis optimization. It is also about 3 times longer than adiabatic analysis-based optimization. Therefore, it can be concluded that the method using 3-level HK model, which is hierarchically constructed on the 2-level HK model of adiabatic best case, is particularly affordable framework for the film cooling hole array optimization problem considering CHT. By extension, the framework used in this study is promising in handling highly-nonlinear or highly-computing resource required problems. In addition, substantially different hole arrangement is obtained as a result of optimization compared to that of adiabatic analysis-based optimization. The second array—ROW1—is moved to ROW0 as close as possible and all the holes are positioned in between the each hole of ROW0. This tendency is similar with the adiabatic result. However, the third array—ROW2—has significantly different shape compared to the adiabatic result. The third arrangement has parabolic shape whose vertex is moved towards the upstream as possible in the design space of ROW2 and slightly towards the shroud direction. Investigating this resultant geometry, the average surface temperature appears in 1050.77 K, which is 49.64 K of temperature reduction compared to that of the baseline. The average overall film cooling

effectiveness increases by 0.058. Additionally, the total mass flow rate passing through the third film cooling hole array is reduced by 28.69%. It can lead the overall cycle efficiency of gas turbine to be improved.

3) When compared the result of CHT-based optimization to that of adiabatic analysis-based optimization, the reason for the shape of third hole array is known by investigating the 3D flow pattern, especially about recirculation and impinging hole effects in the inner cooling passage The shape of second hole arrangement is determined in the way of reducing the area exposed to the hot inlet gas, which is identical to the adiabatic analysis-based optimization In CHT optimized nozzle, the holes located at the mid position on the pressure side are intersecting the rib-turbulators installed at the side wall of the inner cooling passage. This induces strong recirculation to be generated and also renders coolant velocity decelerated. Moreover, it influences the formation of the large recirculation bubble at the upper side of inner cooling passage. Consequently, the coolant passing through the film cooling hole covers broader region behind the nozzle pressure side. Furthermore, the extracted coolant is also spread wider on the blade surface. As a result, when comparing cooling performance to that of adiabatic optimized nozzle, the average surface temperature decreases by 20.02 K and average overall film cooling effectiveness increases by 0.028.

REFERENCES

[1] Chi, Z., Li, X., Han, C., Ren, J., and Jiang, H., "Optimization of the Hole Exit Shaping of Film Holes Without and with Compound Angles for Maximal Film Cooling Effectiveness," ASME TurboExpo, American Soc. of Mechanical Engineers Paper, GT2014-25212, 2014, pp. V05BT13A006-V05BT13A006.

doi : 10.1115/GT2014-25212

[2] Lee, K.-D., and Kim, K.-Y., "Optimization of a Fan-Shaped Hole for Film Cooling Using a Surrogate Model," ASME TurboExpo, American Soc. of Mechanical Engineers Paper, GT2009-59520, 2009, pp. 505–514

doi : 10.1115/GT2009-59520

[3] Nita, K., Okita, Y., Nakamata, C., Kubo, S., Yonekura, K., and Watanabe, O., "Film Cooling Hole Shape Optimization Using Proper Orthogonal Decomposition," ASME TurboExpo, American Soc. of Mechanical Engineers Paper, GT2014-27239, 2014, pp. V02BT39A046-V02BT39A046.

doi : 10.1115/GT2014-27239

[4] Johnson, J. J., King, P. I., Clark, J. P., and Ooten, M. K., "Genetic Algorithm Optimization of a High-Pressure Turbine Vane Pressure Side Film Cooling Array," Journal of Turbomachinery, Vol. 136, No. 1, Sept. 2013, Paper 011011.

doi : 10.1115/1.4023470

[5] Lee, S., Rhee, D.-H., Cha, B. J., and Yee, K., "Film Cooling Performance Improvement with Optimized Hole Arrangements on Pressure Side Surface of Nozzle Guide Vane – Part 1: Optimization & Numerical Investigation," ASME TurboExpo, American Soc. of Mechanical Engineers Paper, GT2016-57975, 2016, pp. V05CT12A010-V05CT12A010.

doi : 10.1115/GT2016-57975

[6] Rhee, D.-H., Kang, Y. S., Cha, B. J., Kang, J.-S., Lee, S., and Yee, K., “Film Cooling Performance Improvement with Optimized Hole Arrangements on Pressure Side Surface of Nozzle Guide Vane – Part 2: Experimental Validation,” ASME TurboExpo, American Soc. of Mechanical Engineers Paper, GT2016-57978, 2016, pp. V05CT12A011-V05CT12A011.

doi : 10.1115/GT2016-57978.

[7] Lee, S., Yee, K., and Rhee, D.-H., “Optimization of the Array of Film Cooling Holes on a High-Pressure Turbine Nozzle,” Journal of Propulsion and Power, Vol. 33, No. 1, Special Section on Pressure Gain Combustion, Jan. 2017, pp. 234–247.

doi : 10.2514/1.B35968

[8] Lee, S., Yee, K., and Rhee, D.-H., “An Optimum Arrangement of the Film Cooling Holes Considering the Manufacturing Tolerance,” Journal of Propulsion and Power, advance online publication, April 2017.

doi : 10.2514/1.B36210

[9] Silieti, M., Kassab, A. J., and Divo, E., "Film Cooling Effectiveness: Comparison of Adiabatic and Conjugate Heat Transfer CFD Models," International Journal of Thermal Sciences, Vol. 48, No. 12, Dec. 2009, pp. 2237-2248.

doi : 10.1016/j.ijthermalsci.2009.04.007

[10] Ghorab, M. G., “Adiabatic and Conjugate Cooling Effectiveness Analysis of a New Hybrid Scheme,” International Journal of Thermal Sciences, Vol. 50, No. 6, June 2011, pp.965-983.

doi : 10.1016/j.ijthermalsci.2011.01.012

[11] Han, Z. H., and Görtz, S., “Hierarchical Kriging Model for Variable-fidelity Surrogate Modeling,” AIAA Journal, Vol. 50, No. 9, Sept. 2012, pp. 1885-1896.

doi : 10.2514/1.J051354

[12] Wilke, G., “Multi-Objective Optimizations in Rotor Aerodynamics Using Variable Fidelity Simulations,” 39th European Rotorcraft Forum (ERF2013). Sept. 2013, pp. 69–72.

[13] Poling, B. E., Prausnitz, B. M., and O'Connell, J. P., The Properties of Gases and Liquids, 5th ed., McGraw-Hill, New York, 2001, pp. 566-569.

doi : 10.1036/0070116822.

[14] Cengel, Y. A., and Ghajar, A. J., Heat and Mass Transfer: Fundamentals and Applications, 5th ed., McGraw–Hill Education, New York, 2014, p.926.

[15] Bardina, J. E., Huang, P. G., and Coakley, T., " Turbulence Modeling Validation,Testing, and Development," NASA TM-110446, 1997.

[16] Lee, K.-D., Kim, S.-M., and Kim, K.-Y., "Multi-Objective Optimization of a Row of Film Cooling Holes Using an Evolutionary Algorithm and Surrogate Modeling," An International Journal of Computation and Methodology, Vol. 63, No. 8, Mar. 2013, pp. 623-641.

doi : 10.1080/10407782.2013.751316

[17] El Ayoubi, C., Ghaly, W., and Hassan, I., "Aerothermal Shape Optimization for a Double Row of Discrete Film Cooling Holes on the Suction Surface of a Turbine Vane," Engineering Optimization, Vol. 47, No. 10, Oct. 2014, pp. 1384-1404.

doi : 10.1080/0305215X.2014.969725

[18] ANSYS14.5 CFX-Solver Theory Guide, ANSYS, Canonsburg, PA, 2012.

[19] Sacks, J., Welch, W. J., Mitchell, T. J., and Wynn, H. P., “Design and Analysis of Computer Experiments,” Statistical Science, vol. 4, No. 4, Nov. 1989, pp. 409-435.

doi:10.1214/ss/1177012413

[20] Simpson, T. W., Mauery, T. M., Korte, J. J., and Mistree, F., "Kriging Models for Global Approximation in Simulation-Based Multidisciplinary Design Optimization," AIAA Journal, Vol. 39, No. 12, Dec. 2001, pp. 2233–2241.

doi : 10.2514/2.1234

[21] Martin, J. D., and Simpson, T. W., "Use of Kriging Models to Approximate Deterministic Computer Models," AIAA Journal, Vol. 43, No. 4, Apr. 2005, pp. 853–863.

doi : 10.2514/1.8650

[22] Toal, D. J. J., Bressloff, N. W., and Kean, A. J., "Kriging Hyperparameter Tuning Strategies," AIAA Journal, Vol. 46, No. 5, May 2008, pp. 1240–1252.

doi : 10.2514/1.34822

[23] Stein, M., "Large Sample Properties of Simulations Using Latin Hypercube Sampling," Technometrics, Vol. 29, No. 2, May 1987, pp. 143–151.

doi : 10.1080/00401706.1987.10488205

[24] Jones, D. R., Schonlau, M., and Welch, W. J., "Efficient Global Optimization of Expensive Black-Box Functions," Journal of Global Optimization, Vol. 13, No. 4, Dec. 1998, pp. 455–492

doi : 10.1023/A:1008306431147

[25] Betró, B., "Bayesian Methods in Global Optimization," Journal of Global Optimization, Vol. 1, No. 1, March 1991, pp. 1–14.

doi : 10.1007/BF00120661

[26] Sasena, M. J., "Flexibility and Efficiency Enhancements for Constrained Global Design Optimization with Kriging Approximations," Ph.D. Dissertation, Univ. of Michigan, Ann Arbor, MI, 2002.

[27] Roache, P. J., Verification and Validation in Computational Science and Engineering, Chapter 6, "Applications of Systematic Grid Convergence Studies and the Grid Convergence Index," Hermosa, Albuquerque, NM, 1998.

[28] Roache, P. J., Fundamentals of Computational Fluid Dynamics, Chapter 19, “The Grid Convergence Index,” Hermosa, Albuquerque, NM, 1998.

[29] Kim, Y., Lee, S., Yee, K., and Rhee, D.-H., “High-to-Low Initial Sample Ratio of Hierarchical Kriging for Film Hole Array Optimization,” Journal of Propulsion and Power, accepted.

doi : 10.2514/1.B36556

초 록

고압터빈 막냉각 기술은 내부 냉각유로의 냉각유체를 막냉각 홀로 방출하여 블레이드 표면에 얇은 막을 형성하여 블레이드를 표면을 보호하는 기술로, 형성된 막으로 인해 블레이드로 유입되는 대류 열전달을 줄이고 전도효과를 발생시키는 블레이드의 내부와 외부의 온도차를 줄여준다. 따라서 전도와 대류 열전달을 모두 고려할 수 있는 복합열전달 해석은 고압터빈 열유동 해석의 정확도 향상에 필수적이다. 하지만 복합열전달 해석은 해석 시간이 많이 소요되기 때문에 복합열전달을 고려한 최적화 연구는 단일 홀 형상 최적화와 같이 비교적 단순한 문제에 대하여 제한적으로 수행되어왔다. 따라서 본 연구는 계산자원의 한계로 단열조건으로만 수행되어왔던 고압터빈 막냉각홀 배열 최적화 문제를 복합열전달을 고려하여 수행하고 이를 분석하는 것을 목적으로 한다. 복합열전달 해석을 수행하는데 계산자원의 부담을 완화하기 위하여 다중정확도 모델링(Variable Fidelity Modeling) 기법 중 계층적 크리깅 모델(Hierarchical Kriging Model)이 결합된 EI(Expected Improvement)기반의 효율적 전역최적점 탐색기법(Efficient Global Optimization)을 도입하였다. 먼저, 다중정확도 모델링 기법을 직접적으로 복합열전달 최적화에 적용하기에 앞서, 단열조건에서 다중정확도 최적화를 수행해봄으로써 효율적인 다중정확도 모델링 기법의 활용을 위한 모호성을 규명하였다. ‘계산자원의 부담을 최대한으로 줄여줄 수 있는 고정확도/저정확도 초기 샘플 비율의 존재성’과 ‘계층적 크리깅 모델의 신뢰성’ 즉, 고정확도/저정확도 초기 샘플 비율이 달라지더라도 계층적 크리깅 모델은 일관되고 신뢰할만한 결과를 도출하는가에 대해서 논의하였다. 그 결과 계층적 크리깅 모델은 고정확도 정보만을 이용하여 수행한 결과와 비교하여 충분히 신뢰할만한 결과를 도출할 뿐만 아니라, 고정확도/저정확도 비율이 달라지더라도 일관된 결과를 도출하고 계산시간 역시 약 40% 줄여준다는

결과를 도출하였다. 해당 결과를 바탕으로 복합열전달을 고려한 고압터빈 막냉각홀 배열 최적화를 수행하였다. 3-레벨의 계층적 크리깅 모델을 이용하여 다중정확도 최적화를 수행하였으며, 그 결과 최적해를 구하는데 까지 소요되는 시간은 약 76.45% 감소하였을 뿐만 아니라 기본형상과 비교하여 49.64 K 줄어든 압력면 평균 온도를 얻고 막냉각효율(ϕ)은 0.058 상승하였다. 한편, 최적해로 도출된 막냉각홀 배열의 형상은 단열조건으로 수행한 최적화 결과와 비교하여 두 번째 홀 배열은 동일한 형상이 도출되었으나 세 번째 홀 배열은 완전히 상이한 결과가 도출되었다. 구체적으로는 세 번째 홀 배열은 꼭지점이 설계범위의 가장 상류에 위치하며 shroud쪽으로 일부 이동하여 위치한 포물선형태를 가졌다. 이러한 형상은 내부 냉각 요소들과 막냉각홀의 위치에따라 변하는 냉각유체의 유동현상을 가능한 넓은 영역의 노즐을 커버할 수 있도록 하는 최적의 조합이다. 홀 배열 형상이 결정되는 이유에 대해서는 본론에서 압력분포, 속도분포, 유선 등을 분석하며 자세히 논의하였다.

주요어 : 항공기용 가스터빈, 고압터빈, 복합열전달 해석, 계층적 크리깅 모델, 막냉각홀 배열 최적화

학 번 : 2015-22733